MR Series FT-Spectroradiometer

Design overview and theory

(Version 3.0)

August 1999

IMZ8948

ABB

ABB Bomem Inc.

TABLE OF CONTENTS

LIST OF FIGURES

LIST OF TABLES

1. INTRODUCTION

This section presents certain theoretical aspects that apply to the MR Series of FT spectroradiometers. It is intended for readers who want to know something about the inner workings of their instrument in order to better understand its applications. Those who are already familiar with FTIR technology may want to use it as a refresher.

1.1 Scope

Chapter 2 outlines the design of the instrument. The underlying concepts presented in this chapter are covered in greater depth in Chapter 3.

1.2 References Documents

[RD1] Peter R. Griffiths and James A. de Haseth, Fourier Transform Infrared Spectrometry, Wiley-Interscience, 1986.

[RD2] B.K. Yap, W.A.M. Blumberg, and R.E. Murphy, Applied Optics, Vol. 21, Page 4176, 1982.

[RD3] Henry E. Revercomb, H. Buijs. Hugh B. Howell, D.D. Laporte, William L. Smith, and L.A. Sromosky, Applied Optics, Vol 27, Page 3210, 1988.

1.3 Abbreviations

ADC	analogue-to-digital converter
DSP	digital signal processor
EMI	electromagnetic interference
FFT	fast Fourier transform
FOV	field of view
FTIR	Fourier transform infrared
FWHM	full-width at half maximum
ILS	instrument line shape
IR	infrared
KB	kilobyte (equals 1024 bytes)
MB	megabyte (equals 1 048 576 bytes)
MPD	maximum path difference (in one direction of the scan arm, or from ZPD)
NEP	noise equivalent power
NESR	noise equivalent spectral radiance

OD	optical density
OPD	optical path difference
RMS	root mean square
RSS	root sum square
SNR	signal-to-noise ratio
ZPD	zero path difference

1.4 Glossary

aliasing	The result of sampling that is too low in frequency to preserve the spectral content of the sampled signal. When signal has a frequency greater than half the sampling frequency, it appears in the sampled signal at a lower frequency.
aperture stop (AS)	The element limiting the size of the cone of radiation which an optical system will accept from an axial point on the source.
calibration	The process by which a relation between a reference and a measurement is established.
coaddition	The coherent addition or signal averaging of interferograms. This is a technique to improve the signal-to-noise ratio by adding successive interferograms with corresponding data points digitised to exactly the same optical retardation. Spectral information will add up faster than noise.
divergence (θ)	The angle under which a point on the primary optics views a source.
extended source	A source filling the field of view (q.v.) of an instrument and radiating in all directions.
field of view (Ω)	The solid angle under which a point on the primary optics views a source.
field stop (FS)	The element which limits the field of view (q.v.) of an optical system.
intensity (I)	The power emitted by a point source (q.v.) into a solid angle. Units are expressed in W/sr. The apparent intensity is the measurement of the intensity of a source without taking atmospheric transmission into account.
irradiance (E)	The power collected by the primary (q.v.) of the radiometer (q.v.) per unit area. Units are expressed in W/cm^2.
point source	A source of infinitesimal dimension and radiating in all directions.
primary	In a telescope, the "primary" is defined as the first focusing mirror which converges incoming radiation into the optical system.
radiance (L)	The power radiated from an object per solid angle unit per unit area. Units are expressed in W/cm^2 sr.
radiometer	An instrument allowing the measurement of radiometric quantities such as E and L, under a given throughput (q.v.). Measurement involves comparing an unknown quantity to a known reference or standard.

spectral intensity (Iσ)	The power emitted by a point source (q.v.) into a solid angle within a specified small spectral interval centred on frequency σ. Units are expressed in W/sr cm^{-1}. The apparent spectral intensity is the measurement of the spectral intensity of a source without taking atmospheric transmission into account.
spectral irradiance (Eσ)	The power reaching the primary (q.v.) of the radiometer (q.v.) per unit area within a specified small spectral interval centred on frequency σ. Units are expressed in W/cm^2 cm^{-1}.
spectral radiance (Lσ)	The power radiated from an object per unit solid angle, per unit area within a specified small spectral interval centred on frequency σ. Units are expressed in W/cm^2 sr cm^{-1}. This unit is used by the spectroradiometer for calibrating the spectrum.
spectroradiometer	An instrument allowing the measurement of radiometric quantities such as Eσ and Lσ, under a given throughput (q.v.). Measurement involves comparing an unknown quantity to a known reference or standard.
throughput (Θ)	The factor quantifying the geometric aspect of power transfer between two objects.
wavenumber (σ)	The optical frequency of light expressed in cm^{-1}.

1.5 Formula and mathematical relations

- The area of an optical element $A = \frac{\pi \times D^2}{4}$ where D is the diameter of the optical element.
- Wavelength in microns is converted from wavenumber by $\lambda = \frac{10{,}000}{\sigma}$.
- The divergence of a telescope is approximated by $\theta = \frac{Dfs}{d}$ where Dfs is the diameter of the field stop and d the focal length of the primary.
- The solid angle of a beam at the entrance of a telescope is approximated by $\Omega = \frac{Afs}{d^2}$ where is the area of the field stop and d the focal length of the primary.

  Afs
- The relation between the solid angle and the divergence is $\Omega = 2\pi(1-\cos\frac{\theta}{2})$. For small angles, e.g. in calculations related to the FOV of telescopes, the following formula provides a good approximation: $\Omega = \frac{\pi}{4}\theta^2$.
- The diameter of an object at a distance d and subtended by a divergence θ is given by $Ds = d\theta$.

- The throughput between two optical elements is given by $\Theta = A\Omega$, *Aas* being the area of the aperture stop and Ω, the solid angle, or divergence, introduced by the field stop. We can approximate Ω by taking the area of the field stop and dividing it by the square of the distance between both stops. The throughput is then expressed by $\Theta = \frac{Afs \times Aas}{d^2}$.
- Converting radiance to irradiance is done by multiplying the radiance by the solid angle of the telescope.
- Converting irradiance to apparent intensity is done by multiplying the irradiance by the square of the distance between the point source and the primary of the telescope.
- Converting apparent intensity to intensity is done by correcting the apparent intensity with an atmospheric transmission spectrum computed by modelling software (Fast Code, Lowtran, Modtran, and others).

2. OVERVIEW OF THE ELECTRO-OPTICAL DESIGN OF THE MR SERIES

2.1 The FTIR technology advantage

There are several technical methods of obtaining spectral information. Most of them rely on the dispersion of light to achieve spectral separation. This can be done with a prism or a grating. In this case the spectral distribution is transformed into a spatial distribution and requires a scanning mirror in one axis. Circular variable filter radiometers are also currently used, but spatial/spectral smearing effects add to the other drawbacks of this method.

The Fourier transform (FT) spectrometer does not rely on spatial dispersion, but rather on time dispersion of the spectral information. This limits the number of moving components and provides a more reliable observation geometry. This is a further advantage that can be added to the three "classical" advantages of FT spectrometry over dispersive spectrometry:

- Multiplexing—all wavelengths fall on the detector at all times
- Throughput—the aperture vs resolution limitation is reduced
- Wavelength accuracy—the internal laser ensures stability in ppm levels

In practical terms, the superiority of the FTIR spectroradiometer can be seen most clearly in its ***high spectral resolution*** and ***broadband capability***.

The throughput and thus the sensitivity of FT spectroradiometers is superior to that of dispersive spectroradiometers; a tendency which increases as spectral resolution is increased.

FT spectroradiometers have inherent broadband capability. When no optical filtering is used, the spectral bandwidth of the instrument is the same as that of the detector used, for example 1 to 5.5 μm in the case of an InSb detector. It is also important to note that there is no time penalty when acquiring a large bandwidth as opposed to a narrow one.

Finally, the most useful characteristic of an FT spectroradiometer is its ***flexibility***. The spectral resolution of FT spectroradiometers can be instantly changed by computer. Also, because of the complete separation of spectral information (performed in the time domain) and spatial information (performed in the spatial domain), the FOV configuration of the instrument can be changed in the field, simply by changing telescope modules.

2.2 Design of the MR system

The MR system consists of three conceptual subsystem units: the optomechanical subsystem, the electronic subsystem, and the data processing and control subsystem. The optomechanical and electronic subsystems are located together inside the radiometer unit itself. The data processing and control subsystem is packaged in one enclosure.

2.2.1 The MR interferometer

At the heart of the MR spectroradiometer is a Michelson interferometer. The operation of the interferometer can be understood as a mechanical chopper for which the chopping frequency is a function of wavelength. Intensities for all wavelengths are added together linearly, each with its distinct chopping frequency; these intensities are subsequently decomposed into a spectrum by FT computation.

Figure 1 shows the path of the infrared radiation inside the interferometer. The incoming collimated beam from the scene hits the lower portion of the beamsplitter at a 45° angle. The transmitted and reflected beams hit the lower halves of the hollow corner cube retroreflectors and the return beams are shifted upward because of the reflections inside the corner cubes. The beam then recombines in the upper portion of the beamsplitter. Two beams exit the interferometer, one at 90° to the incoming scene radiation (output beam A) and one back to the scene but displaced vertically (output beam B). In the standard MR100, only one of the output beams is used. However, it is possible to introduce two output beams simultaneously and to place detectors where the two beams exit. This feature is optional with the MR100 but standard with the MR200.

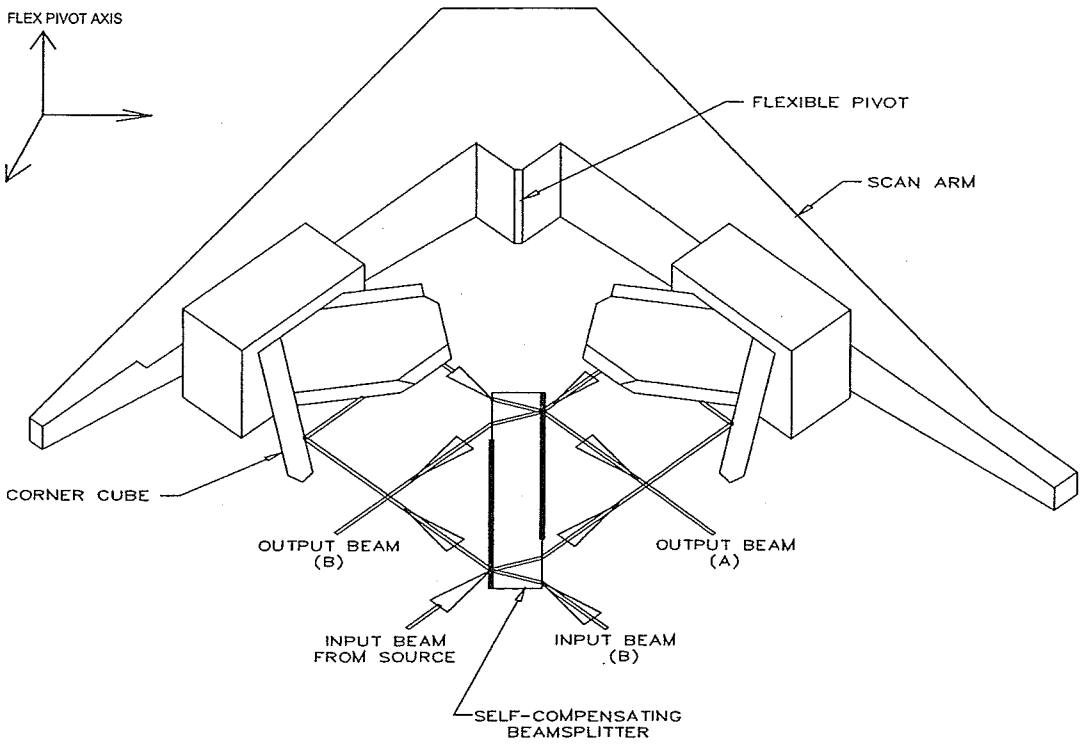

Figure 1. Diagram of the MR Series Michelson interferometer

There is an interesting relation between both outputs for one of the inputs. The unmodulated input signal from the scene will result in two identical modulated signals (interferograms) although one is inverted with respect to the other. This can be understood in terms of energy balance where:

modulated output B = DC input from the scene - modulated output A

Using the chopper analogy, we could say that the chopper has reflective blades such that when the beam does not go in between two blades, it is reflected to another output. Overall, the sum of both outputs will always give a DC constant: the unmodulated power of the source.

There is a similarly interesting relation between both inputs for a given output port. This relation is defined as optical subtraction. Suppose that both inputs are gathered from the same scene. We know that the contribution of one of the inputs will translate into a positive interferogram at the detector port. By analogy with the dual detector output, the second input port will contribute to an equal but inverted interferogram such that the sum of the two ports is a DC intensity: whence the optical subtraction of the modulated parts of the signal. Here, the chopper analogy suggests that both sides of the chopper are reflective and that both sources, symmetrically located at a 45° angle with respect to the chopper blades, are chopped 180° out of phase respectively.

The most common configuration of a Michelson interferometer uses a compensator plate to equalise the amount of beamsplitter material that each beam in the interferometer arm passes through. In this conventional flat mirror design, each beam undergoes 4 passes through the compensator and beamsplitter substrate material. At each interface, reflection losses occur which lower the overall efficiency of the interferometer system. In the MR Series interferometer, the IR beam in each arm undergoes the same number of passes through the beamsplitter substrate material. This design

eliminates the need for a compensator plate and minimises the reflection losses in the system, thus increasing the overall efficiency.

The MR series interferometer is modular. The scan arm, cube-corner retroreflectors, interferometer, white light source, laser, laser power supply, and laser detectors are combined into one prealigned module within the spectroradiometer housing. This modularity in the design allows for fast and easy repair, if needed, by replacement of parts on the module or by replacement of the prealigned interferometer module itself.

Digitisation of the interferogram requires precise monitoring of the optical path in the interferometer. Like most commercial FTIR spectrometers, the MR spectroradiometer incorporates, in the interferometer module, an internal He-Ne laser emitting at 15798 cm^{-1}. This monochromatic laser radiation gives a sinusoidal interferogram which is detected and digitised to yield an optical path difference (OPD) feedback. Conversion of the infrared signal from analogue to digital is triggered at the zero crossings of the laser fringe signal. However, a single laser signal is not sufficient for two reasons: First, the direction in which the scan arm moves must be detected to correctly monitor and control the optical speed of the interferometer. Second, the laser signal itself does not give a reference point from which the location of the zero path difference (ZPD) can be determined.

To solve the first problem, quadrature laser signals are used to find the scanning direction of the scan arm. The incident beam is randomly polarised and can then be seen as two different but collinear beams, one horizontally polarised and the other vertically polarised. The beams are separated and recombined in the interferometer much like the infrared beam, but in one of the arms, the beams are transmitted through a special birefringent optical material. The index of refraction of this material has the interesting characteristic of giving a different optical retardation for the horizontally and vertically polarised beams. This means that an OPD is introduced between the two polarisations. At the output of the interferometer, these two polarisations are separated one from the other and directed to different detectors. When the laser intensity at these two detectors is monitored, a shift can be seen between the two observed sinusoidal waveforms. The digital electronics recognises the relative phase relationship generated by moving the mirrors in direction 1 or direction 2 and can then determine direction from these two signals. This logic is rigorous. Millions of scans can be executed without a single fringe count error.

The second problem necessitates some kind of other reference in order to find the reference point for the interferometer, the ZPD location. This is done with a temporary, white-light system. Each time the MR spectrometer is turned on or when excessive vibration causes the unit to reset itself, a small visible source—a light bulb—lights up, and this radiation goes through the interferometer using the portion of the beamsplitter used by the laser. The detected white light interferogram is a sharp spike because of the high optical frequency content and broadband emission of the visible source. The signal is detected and used to determine the position of the ZPD. Once the system has identified this location, the white-light source turns off until the system is reset again.

2.2.2 The MR system's optical layout

The location of optical elements in the MR system is presented in figure 2. (Note that figure 2 is an MR100 type radiometer, the MR200 has certain differences) Each of these elements is labelled with a number, followed by a two-letter code identifying its function in the system. Elements labelled Fs, As and Tr represent Field Stop, Aperture Stop, and Transfer optics (window or flat mirror) respectively. The entire optical system has only one field stop and one aperture stop. However, any of the elements labelled Fs and As can act as the field stop and the aperture stop respectively. We will define below which optical elements act as the field and aperture stops for the optical system.

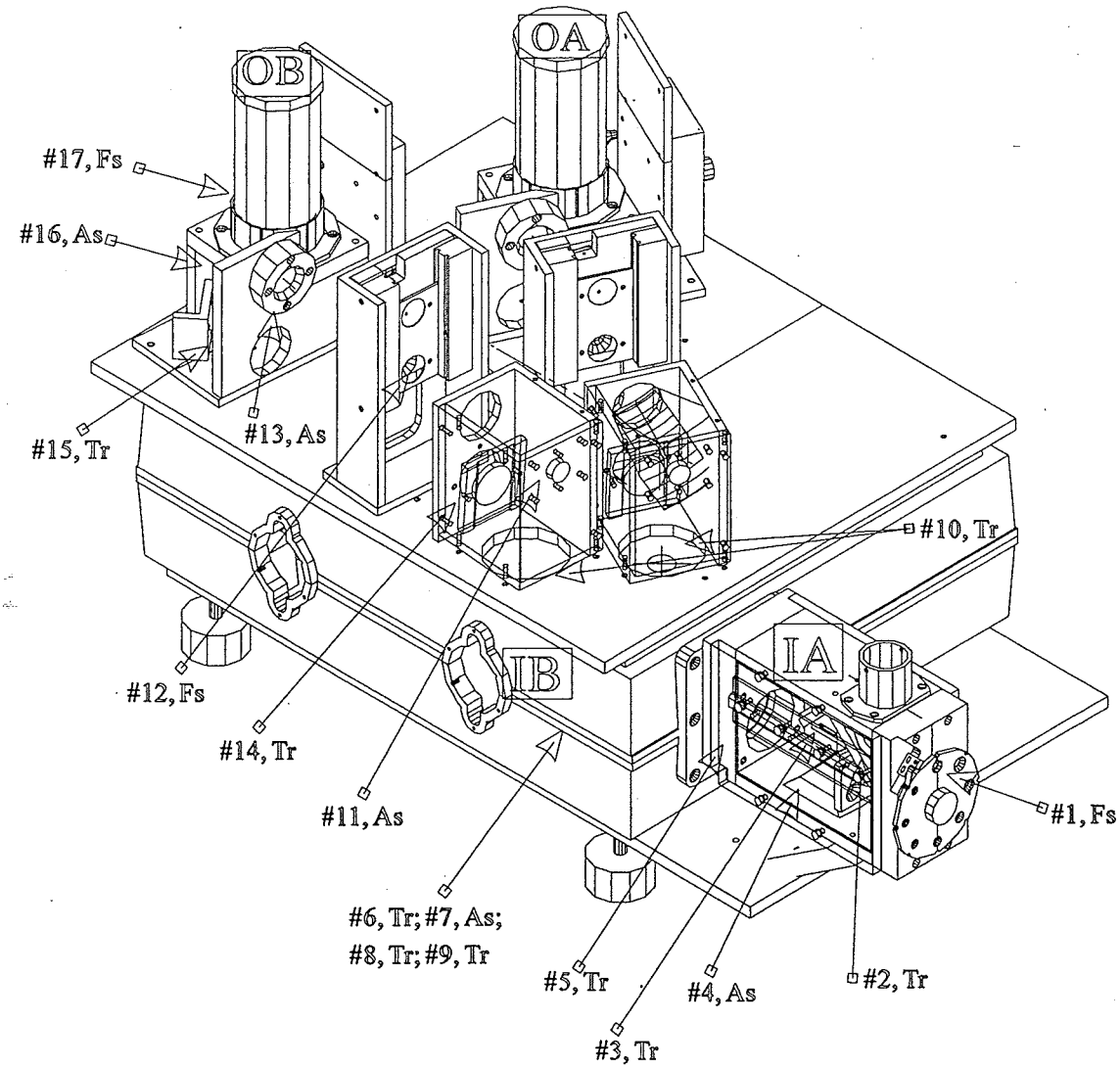

Figure 2. Location of optical elements in the MR system

The optical system ray tracing (layout) is presented in figure 3 and shows the optical beam from the field stop of the system to the detector.

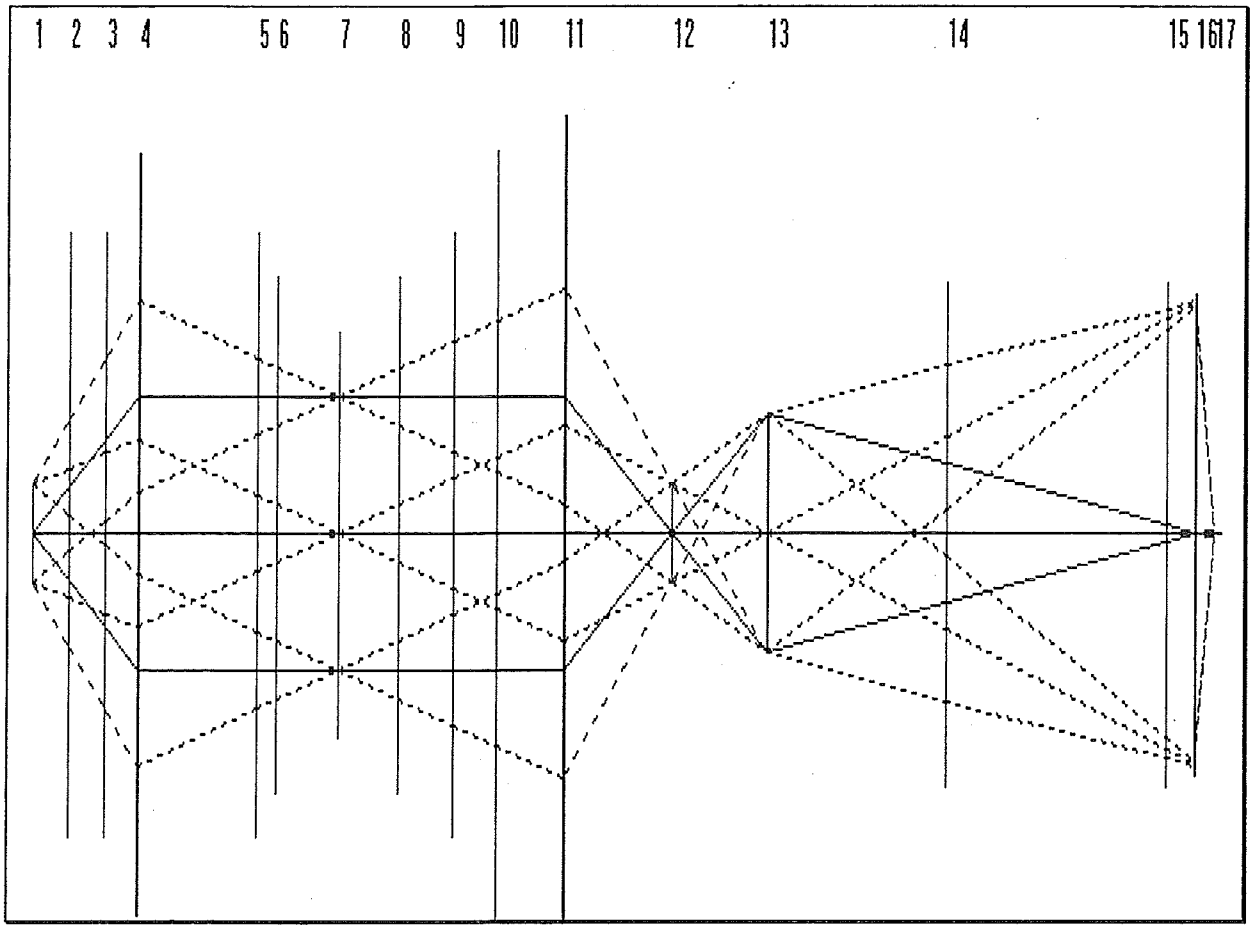

Figure 3. Optical layout of the MR system

Elements numbered 1 to 5 in figure 2 represent optional input optics referred to as the "input collimator". Figure 4 shows a more detailed view of the input collimator.

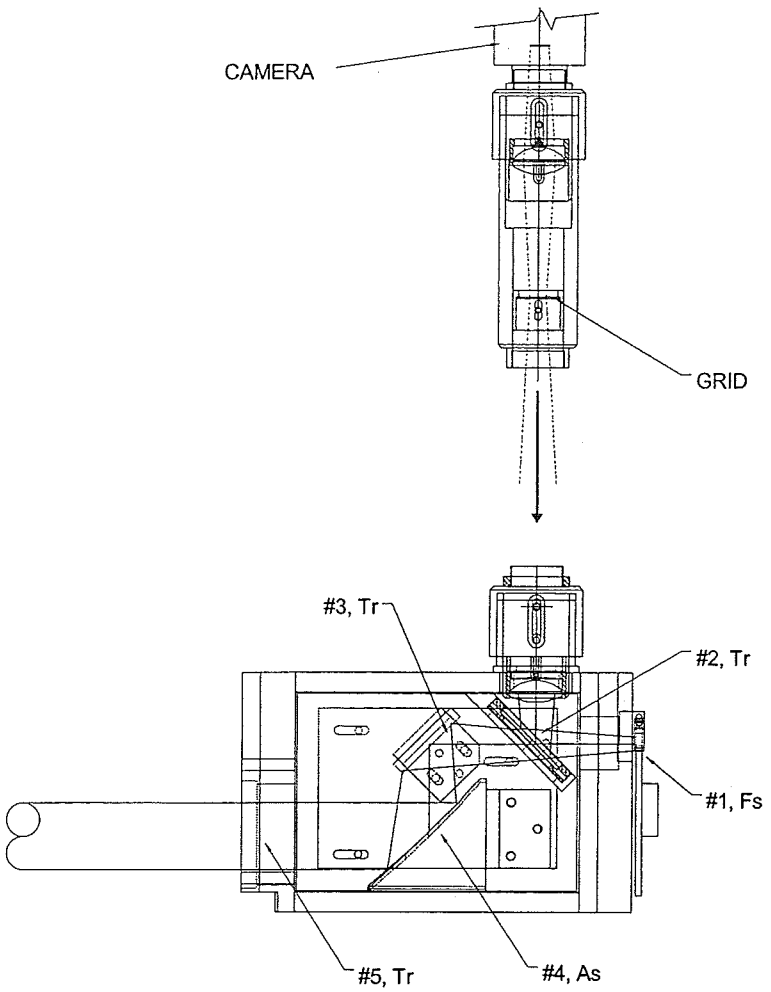

Figure 4. Input collimator with optional video camera accessory

The input collimator is designed to accommodate various types of input telescopes. It can also contain a dichroic that is used to divert the visible image of the scene to an ocular or to a CCD video camera. An optional module can be added to provide a reference grid superimposed on the scene when a video camera is used.

Element 1 represents the field stop of the system; as does element 12 when the input collimator is not installed.

Elements 6, 7, and 8 represent the interferometer and element 9 is a 45° upward folding mirror.

Elements 11 to 16 make up the radiometric output optics of the instrument. The output optics are located on the instrument top plate. The optical path through the output optics is described in figure 5.

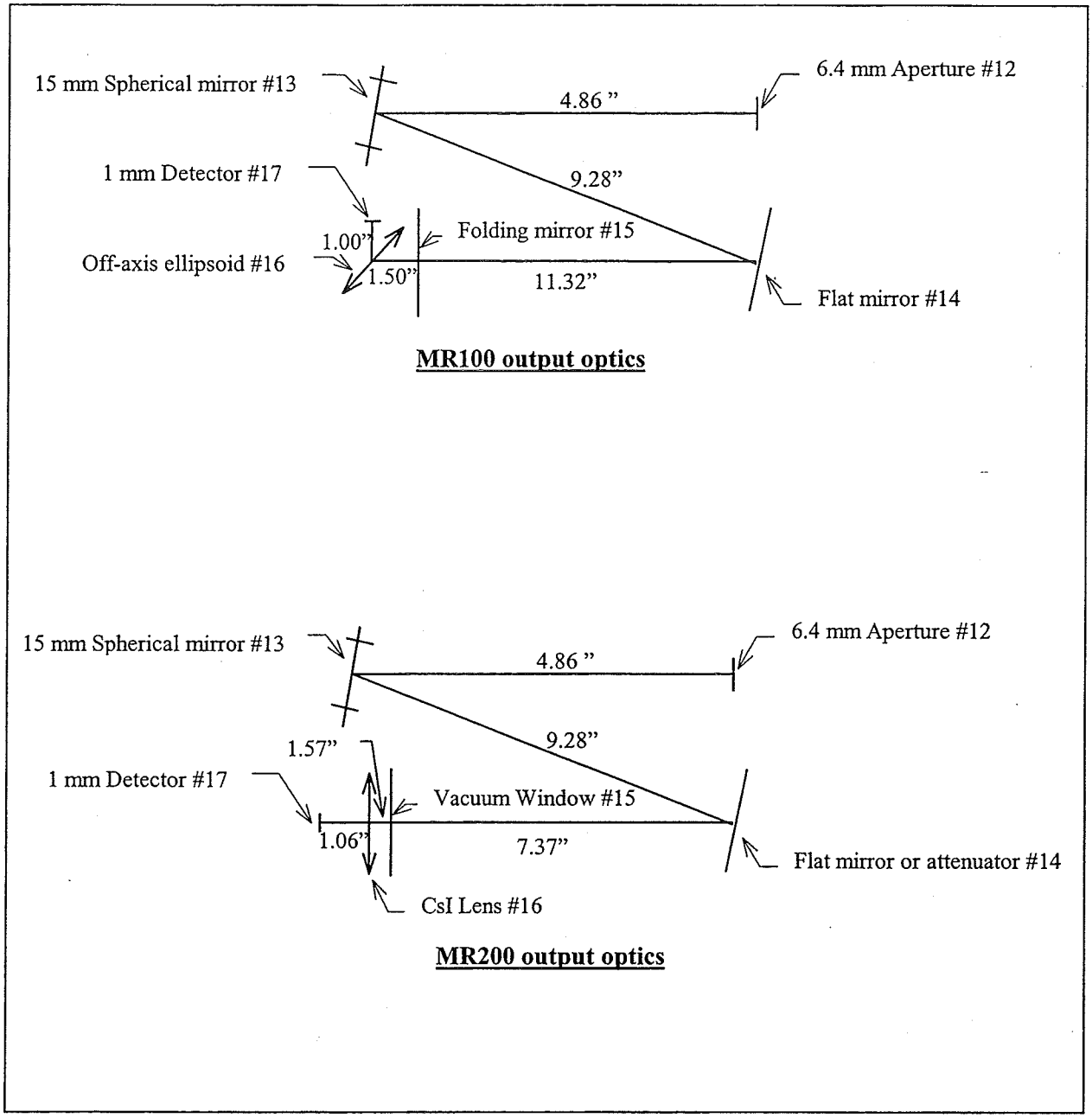

Figure 5. Output optics of the MR systems

Element 13 (the spherical mirror) which represents the instrument aperture stop is imaged on the detector by element 16 an off-axis ellipsoid mirror on the MR100 or a plano-convex CsI lens on the MR200. Elements 13, 15 and 16 are mounted onto the detector assembly as shown in figure 6 for the MR100 and in figure 7 for the MR200.

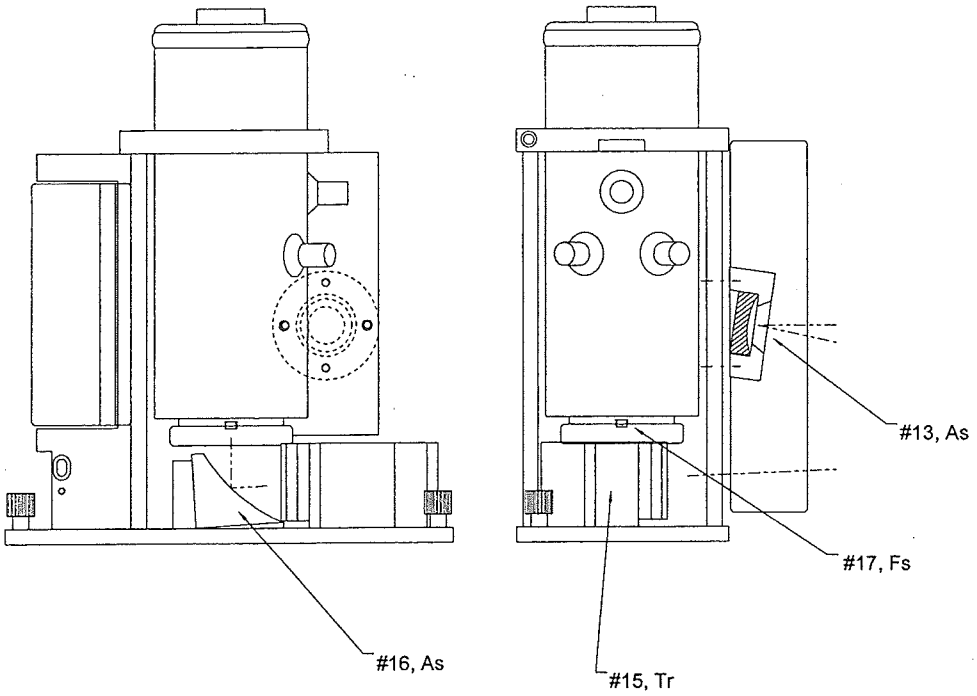

Figure 6. MR100 type detector module

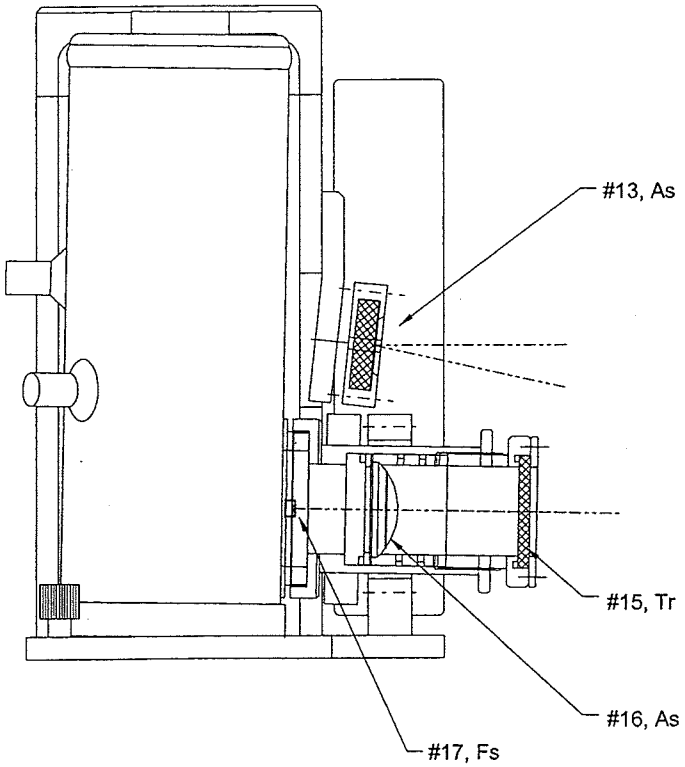

Figure 7. MR200 type detector module

Element 13 also images the field stop (element 12) onto the surface of element 16 to reduce the amount of vignetting. This optical arrangement reduces FOV nonuniformity by uncoupling the field (a representation of the scene) from the detector. This is important because certain detector elements are highly non-uniform over their surface.

Element 14 is normally a flat mirror but it can optionally be replaced by an attenuator system on the MR200. This system allows switching from a normal front coated gold mirror to a BaF_2 reflective attenuator. The advantage of this system is that it allows calibrating the instrument without changing the field stop. The attenuator reflects about 3% of the infrared light incident upon it.

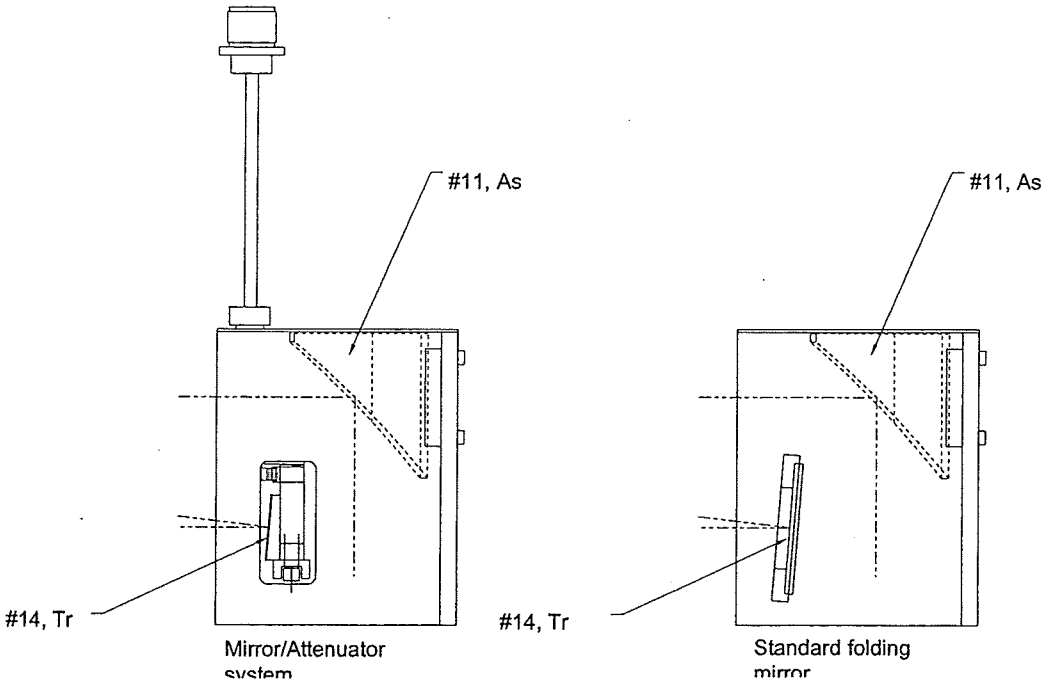

Figure 8. Transfer optics

More precise information about the optics just described is presented in tables 1 and 2.

Table 1. Description of optical components MR100

Element	Description	Next element (inches)	Focal length (inches)	Radius (inches)
1	Entrance field stop (aperture wheel)	1.906	-	0.125
2	Dichroic for boresighting (optional)	1.906	-	0.750
3	Flat folding mirror	1.687	-	0.750
4	Collimator, paraboloid	6.090	5.500	0.940
5	Input window	1.030	-	0.750
6	Beamsplitter (1^{st} reflection)	3.180	-	0.640
7	Corner cube	3.170	-	0.502
8	Beamsplitter (2^{nd} reflection)	2.810	-	0.640
9	45° upward folding mirror	2.250	-	0.750
10	Output window	3.490	-	0.950
11	Focusing mirror, paraboloid (same as #4)	5.500	5.500	1.030
12	Field stop (same as #1)	4.860	-	0.125
13	Field mirror, spherical mirror (the aperture stop of the optical system)	9.280	3.937	0.300
14	Flat folding mirror	11.320	-	0.625
15	Flat folding mirror	1.500	-	0.625
16	Ellipsoidal mirror	1.000	1.000	0.600
17	Detector	-	-	0.020

Table 2 Description of optical components MR200

Element	Description	Next element (inches)	Focal length (inches)	Radius (inches)
1	Entrance field stop (aperture wheel)	1.906	-	0.125
2	Dichroic for boresighting (optional)	1.906	-	0.750
3	Flat folding mirror	1.687	-	0.750
4	Collimator, paraboloid	6.090	5.500	0.940
5	Input window	1.030	-	0.750
6	Beamsplitter (1^{st} reflection)	3.180	-	0.640
7	Corner cube	3.170	-	0.502
8	Beamsplitter (2^{nd} reflection)	2.810	-	0.640
9	45° upward folding mirror	2.250	-	0.750
10	Output window	3.490	-	0.950
11	Focusing mirror, paraboloid (same as #4)	5.500	5.500	1.030
12	Field stop (same as #1)	4.860	-	0.125
13	Field mirror, spherical mirror (the aperture stop of the optical system)	9.280	3.837	0.300
14	Flat folding mirror (or optional BaF_2 attenuator)	7.375	-	0.625
15	Vacuum window	1.567	-	0.625
16	CsI plano-convex lens	1.058	1.000	0.531
17	Detector	-	-	0.020

2.2.3 Data acquisition and processing

As mentioned earlier, the raw data measured by an FT spectroradiometer is temporal, not spectral. The data acquired while the system is scanning represents the power radiated from the scene modulated with itself for different phases (called the "path difference"). The result is the sum of monochromatic sources over a given spectral range and is called an interferogram.

As with other types of spectrometers, the radiation power measured by the optical system is converted by a detector into an electrical signal. This signal is amplified and conditioned by means of electrical filtering as illustrated in figure 9. The amplifier gains can be changed to accommodate the intensity of

the source. On the MR200 both the first stage and second stage gains can be modified and all gains are controlled by the computer. The first stage gain can be switched either between 1 and 4 or between 1 and 16 depending on the type of detector module. The MR100 only has variable gain on the second stage, the gain is changed by using a rotary switch.

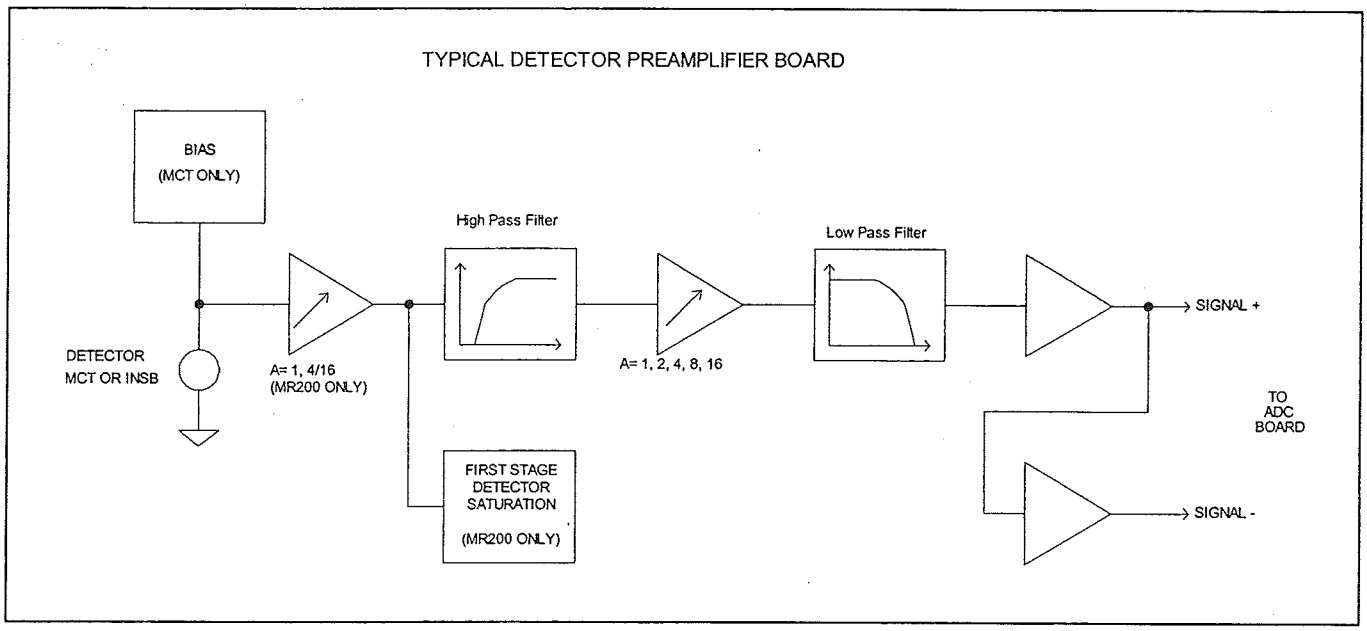

Figure 9. Detector and preamplifier

The signal is then transported under a differential mode, preserving the SNR from electrical pick-up noise, and digitised by means of analogue-to-digital converter circuitry as illustrated in figure 10.

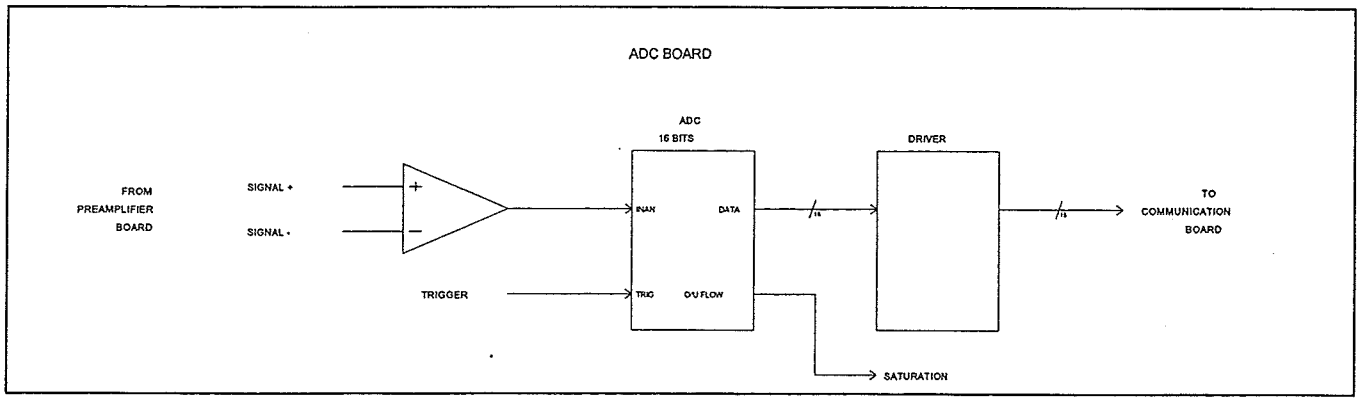

Figure 10. Analogue-to-digital converter

Most of the acquisition control is done by a controller located inside the MR system. Its role is to interpret the commands from the host computer and to ensure synchronisation of the different optical elements of the Radiometer.

A diagram of the MR200 Series architecture is presented in figure 11; the interconnections between the different modules are as illustrated.

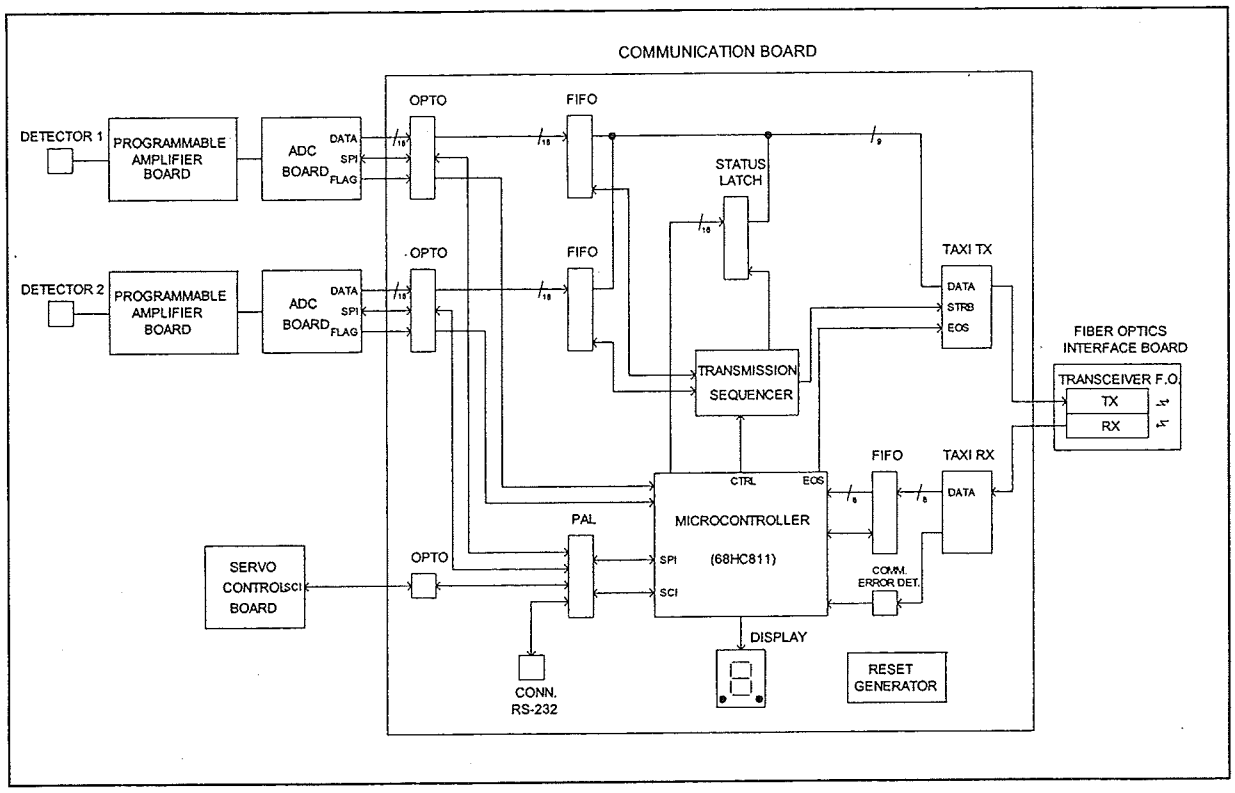

Figure 11. The MR200 data processing architecture

The servo control board is a module which ensures the scanning mechanism speed control, an important factor in spectral fidelity. The architecture of the servo control is illustrated in figure 12.

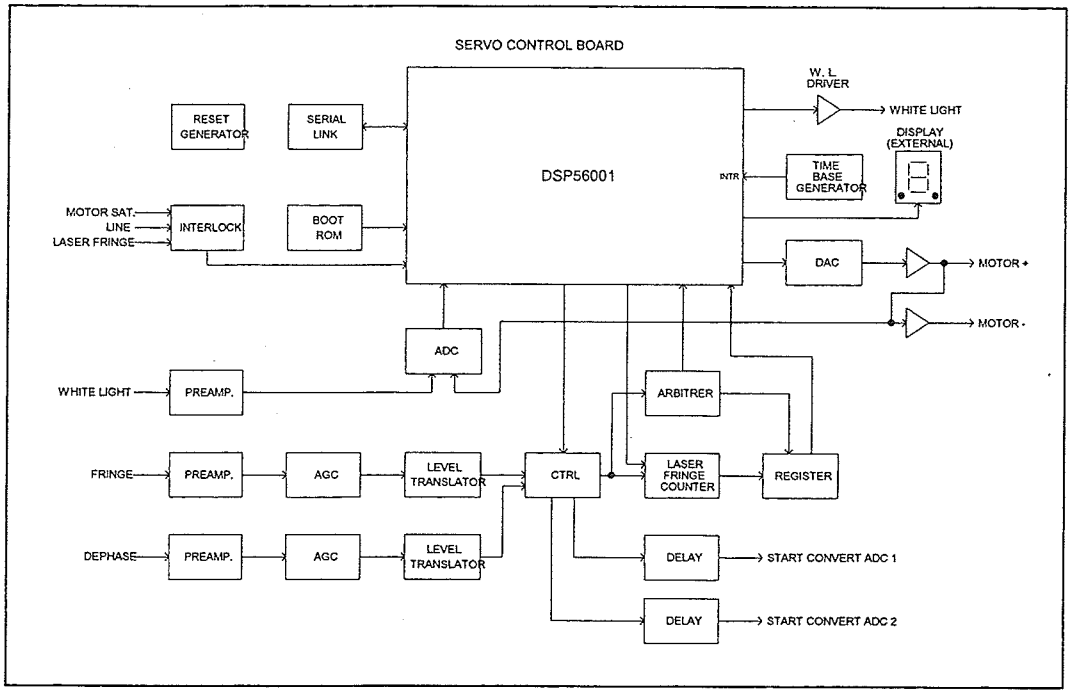

Figure 12. MR200 servo control circuit

The servo control module uses the fringe pattern (a sine wave) of a He-Ne laser which is directed into the interferometer module and collected by dedicated sensors (FRINGE and DEPHASE). The displacement of the scanning mechanism can be monitored from the fringe signal, and this information used to control the motors (voice coils) to ensure proper speed stability. The motors are located at each end of the scanning mechanism.

One function of the control board is to trigger the analogue-to-digital converters to sample the signal. The trigger is determined from the internal He-Ne fringe pattern (zero crossing) and compensates for speed instability by the addition of a delay which corresponds to the response time of the IR detector. This is done to match the time at which the fringe zero crossing is detected to the time this signal is present at the detector output. Both positive and negative fringe crossovers can be used to double the sampling frequency.

This doubling, called "oversampling", is done in order to avoid aliasing when operating above one half of the He-Ne laser frequency (7899 cm^{-1}). In oversampling mode, the MR system features a free spectral range from 0 to 15 798 cm^{-1} (633 nm). In practice, and with the proper detector and ZnSe optics, MR systems will cover the region between 550 and 14 000 cm^{-1} (700 nm and 19.5 microns).

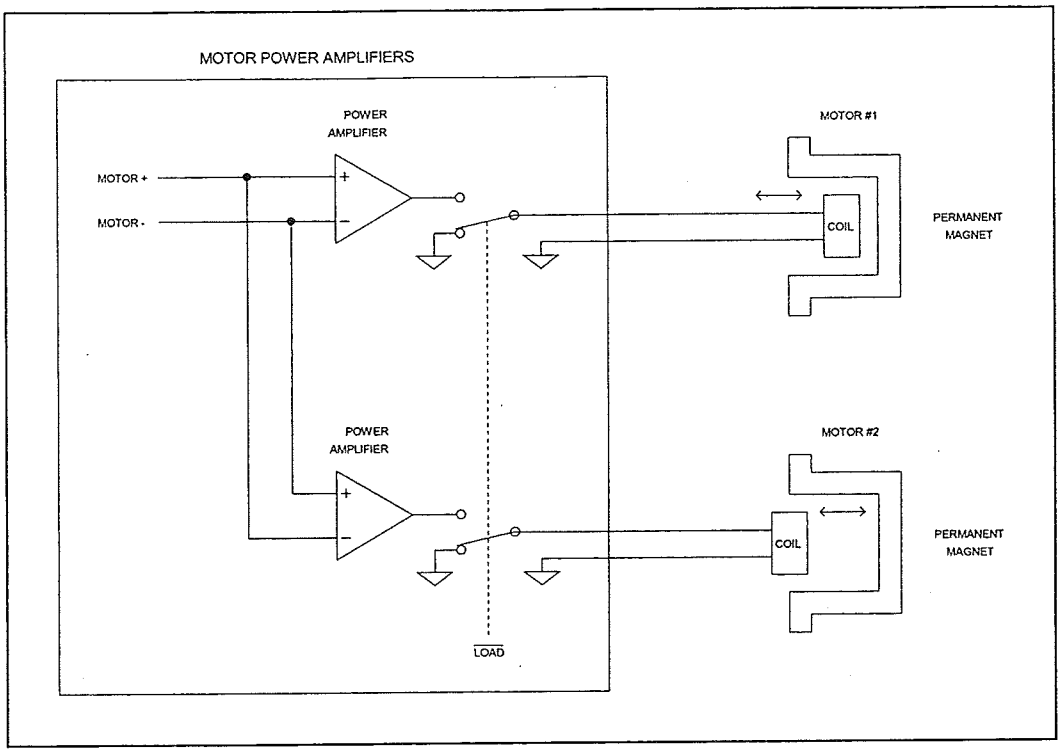

Figure 13. MR200 motor driving circuit

The architecture of the MR100 Series is similar to that of the MR200, but simpler because of less-demanding engineering requirements, such as high-speed scanning and high-data throughput. The two Series differ in the following:

- The MR100 control module supports only one ADC, while the MR200 supports two. In the MR100, operation with two detectors is carried out by adding a slave control board and a second RS-422 communication link.
- The ADC of the MR100 is included as part of the control board, but is integrated in the detector module of the MR200.
- The PID servo control of the MR100 is analogue, while that of the MR200 is digital.
- Data transmission to the host computer is done via an RS-422 serial link for the MR100 Series and via optical fibre for the MR200 Series.
- Detector preamplifier gain control is manual with the MR100, it is remote with the MR200. The MR200 can also be operated in auto-gain mode. When this is done the instrument automatically picks the best gain for the current scene.
- One motor is used to power the scanning mechanism in the MR100, as opposed to two in the MR200.

The MR system interfaces with the host computer by an acquisition board which includes the following components:

- a high-speed processor (Motorola DSP96000)
- a dynamic random access memory buffer for data storage

- a static RAM buffer for high-speed calculations
- an IRIG-B RS-232 interface
- an I/O interface with the computer bus
- an RS-422 interface for the MR100 and a fibre optic interface for the MR200

A diagram of the interface board architecture is presented in figure 14.

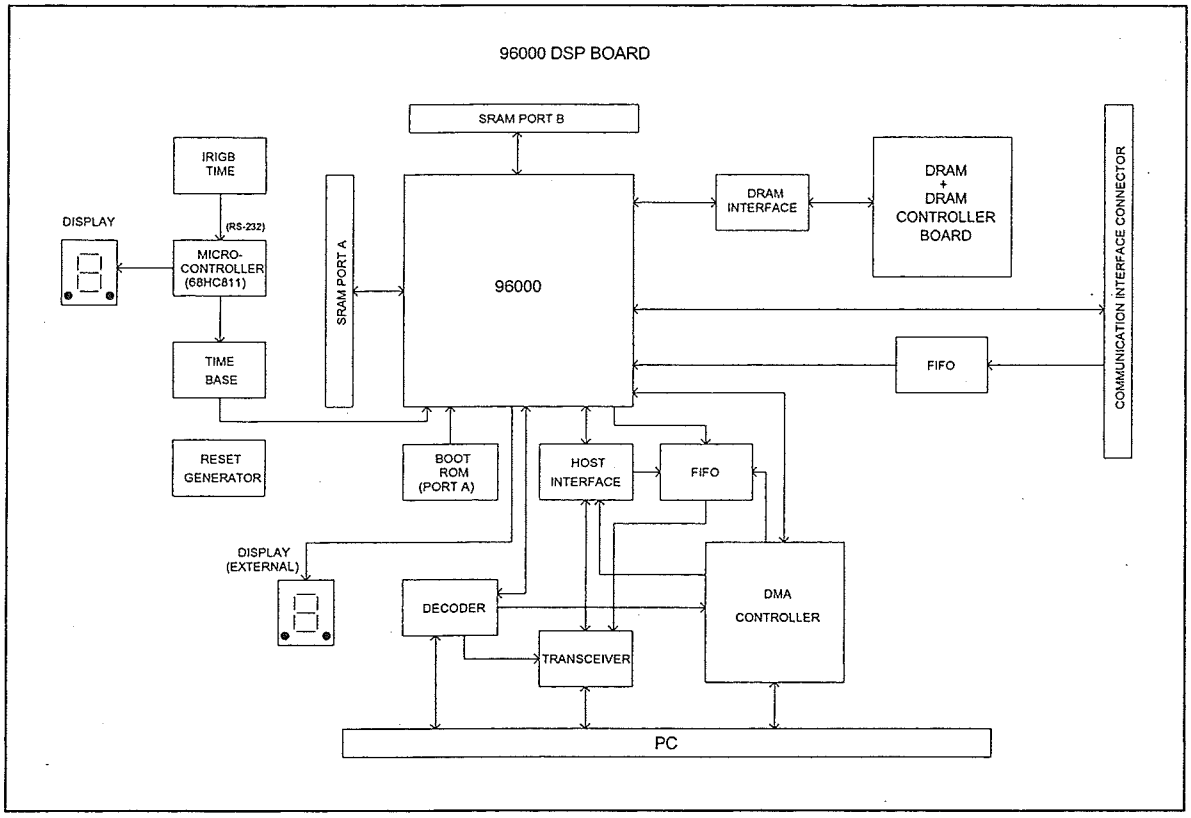

Figure 14. MR to PC interface board

The internal operation is as follows:

- The host computer acquisition software instructs the DSP to initiate data acquisition. MR systems are constantly scanning, and therefore acquisition will start at the next valid scan.
- Data points are stored by the DSP in the DRAM buffer. In kinetic mode, interferograms are stored at different locations in DRAM until the number of scans requested is completed. In coaddition mode, the memory buffer is used to add interferograms together for signal averaging to improve the SNR.
- When interferogram data is requested from the DSP, the data points are transferred from the DRAM directly onto disk; whereas when spectral data is asked for, it is first apodised and Fourier transformed by the DSP, and then stored to disk.

The conversion to meaningful radiometric data is achieved by a certain amount of postprocessing which includes Fourier transform and radiometric calibration using stored data measured from calibrated sources under a known optical geometry.

2.2.4 Software philosophy

Two software modules are provided with MR systems: a DOS-based acquisition module—Research Acquire; and a Windows-based data manipulation and processing module—Bomem GRAMS.

Research Acquire provides the functions necessary for general MR applications. It includes functions to acquire raw interferograms, uncalibrated spectra, radiometric reference spectra using calibrated sources, and calibrated spectra. It also acquires FTIR-type data in transmission, such as raw, reference, transmittance and absorbance spectra, which can be useful for quick diagnostics in such things as the measuring of stability, the transmission capacity of optical filters, and a general examination of the spectral content of the source observed.

Research Acquire also includes a basic display system and a set of postprocessing functions to perform radiometric calibration, conversion to temperature units, integration over programmable bands, computation of theoretical Planck functions, addition, subtraction, multiplication, and ratios.

Bomem GRAMS software is used to view, process, and organise data. It allows easy data and graphics exchange with other Windows applications such as spreadsheet and word processors. Data processing capabilities are fast and accurate. It includes a built-in programming language, Array Basic, so that advanced users can modify existing algorithms or create new ones for the individual requirements of specific experiments.

2.2.5 Data flow outline

Data acquisition involves notions of size, type, and transfer rate. These are functions of scanning speed, spectral resolution, and spectral range. Temporal and spectral data represent the two types involved in an FT spectroradiometer; these two types are linked by the Fourier transform.

The following points will help the user understand how data is generated and help plan an experiment by taking data flow into account.

- The scan length is a function of resolution.
- All wavelengths are acquired simultaneously whatever the scan length is.
- MR systems acquire double-sided interferograms.
- The sampling rate is a function of the scanning speed and of the number of samples per fringe or oversampling factor.
- The maximum observable spectral range is determined by the oversampling factor. In the MR series the oversampling factor can be 1 (no oversampling) or 2, this provides for spectral ranges of 0 to 7899 cm^{-1} and 15798cm^{-1} respectively.
- Each data point is stored as a 16 bit number. Coadding or signal averaging is done with 32 bit numbers.
- The maximum number of interferograms which can be recorded in kinetic mode depends on the size of the DRAM buffer. This is 4 MB (expandable to 64 MB) in the case of the MR100, and 64 MB in the MR200.

- The required scanning speed is dictated by how fast an event is to be resolved, it is limited by the ADC speed, the detector response time, and the throughput of the electronics, including the communication links. It is 1 cm/s in the MR100 and 25 cm/s in the MR200.

The following table summarises the above items and presents data size and flow according to resolution, oversampling factor, and speed for both the MR100 and 200 Series.

Table 3. MR systems data flow

Instrument	Optical scanning velocity (cm/s)	Fringe rate (Hz)	Oversampling*	Resolution (cm^{-1})	Points per interferogram	Observation time (s)	Turn-around time (s)	Scans per second	Maximum acquisition time (s)
MR100	1	15 798	1	16	2 048	0.129	0.15	3.6	272
MR100	1	15 798	1	8	4 096	0.253	0.15	2.5	200
MR100	1	15 798	1	4	8 192	0.506	0.15	1.5	164
MR100	1	15 798	1	2	16 384	1.012	0.15	0.8	144
MR100	1	15 798	1	1	32 768	2.025	0.15	0.5	136
MR100	1	15 798	2	16	4 096	0.126	0.15	3.5	136
MR100	1	15 798	2	8	8 192	0.253	0.15	2.5	100
MR100	1	15 798	2	4	16 384	0.506	0.15	1.5	80
MR100	1	15 798	2	2	32 768	1.012	0.15	0.9	72
MR100	1	15 798	2	1	65 536	2.025	0.15	0.5	68
MR200	25	375 000	1	16	2 048	0.005	0.01	64.6	242
MR200	25	375 000	1	8	4 096	0.010	0.01	47.8	163
MR200	25	375 000	1	4	8 192	0.021	0.01	31.4	125
MR200	25	375 000	1	2	16 384	0.042	0.01	18.6	104
MR200	25	375 000	1	1	32 768	0.085	0.01	10.3	95
MR200	25	375 000	2	16	4 096	0.005	0.01	64.6	121
MR200	25	375 000	2	8	8 192	0.010	0.01	47.84	82
MR200	25	375 000	2	4	16 384	0.021	0.01	31.4	62
MR200	25	375 000	2	2	32 768	0.042	0.01	18.6	52
MR200	25	375 000	2	1	65 536	0.085	0.01	10.2	47

* 1 provides a range of 0 to 7 899 cm^{-1} and 2 provides a range of 0 to 15 798 cm^{-1}

The maximum allowed acquisition time is calculated for one detector, when two detectors are used simultaneously, the time is halved.

3. RADIOMETRIC AND SPECTRAL THEORY

Although this chapter is meant to be purely theoretical, efforts are made to illustrate the theory with examples pertaining to the MR system whenever possible.

3.1 Sensitivity

The sensitivity of a system is its ability to transform input radiance into signal form. This sensitivity is a function of many parameters such as noise, transmission, modulation, throughput, and detector responsivity. The important quality of the system is its ability to distinguish the signal from the noise. This is expressed in terms of its signal-to-noise ratio (SNR). In the context of detection, it is often stated that the *signal can be detected when its amplitude is at least three times the peak noise amplitude.* Figure 15 shows the computational steps used to predict the signal-to-noise ratio of an interferometer system. The computations presented here were performed using in-house simulation software. The evaluation of the SNR is described in the following sections.

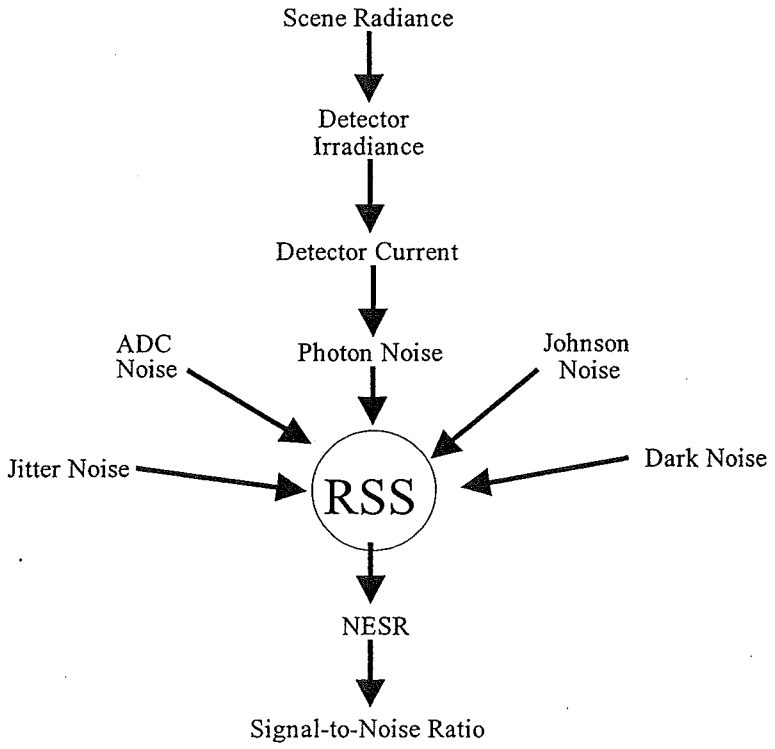

Figure 15. Signal-to-noise ratio computation steps

3.1.2 Scene spectral radiation

Figure 16 shows the radiation from an ideal blackbody source at various temperatures between 100°C and 1600°C on a logarithmic scale. It can be seen that the dynamic range requirement of the system is quite large, spanning almost four orders of magnitude at 3.5 µm.

Spectral radiance from the scene is given by Planck's equation:

$$L(\sigma) = \frac{C_1 \sigma^3}{\exp\left(\frac{C_2 \sigma}{T}\right) - 1} \qquad (1)$$

where

C_1 = 1.191 × 10-12 W/ (cm^2 sr $(cm^{-1})^4$) is the first radiation constant,

C_2 = 1.439 K cm is the second radiation constant,

σ is the wavenumber in cm^{-1},

T is the temperature of the scene in K,

$L(\sigma)$ is the radiated power density or *spectral radiance* in W/(cm^2 sr cm^{-1}).

This version of Planck's equation expressed in wavenumbers is different from the usual equation expressed in wavelengths:

$$M(\lambda) = \frac{C_1 \lambda^{-5}}{\exp\left(\frac{C_2}{\lambda T}\right) - 1} \qquad (2)$$

The difference comes from the fact that Planck's function is a power density. Because $\sigma = 1/\lambda$, the infinitesimal wavenumber element $d\sigma$ is equal to $-d\lambda/\lambda^2$. Thus:

$$\int_{\sigma_1}^{\sigma_2} L(\sigma) \quad d\sigma = \int_{\lambda_1}^{\lambda_2} M(\lambda) \quad d\lambda \qquad (3)$$

and the apparent disagreement between equations 1 and 2 disappears.

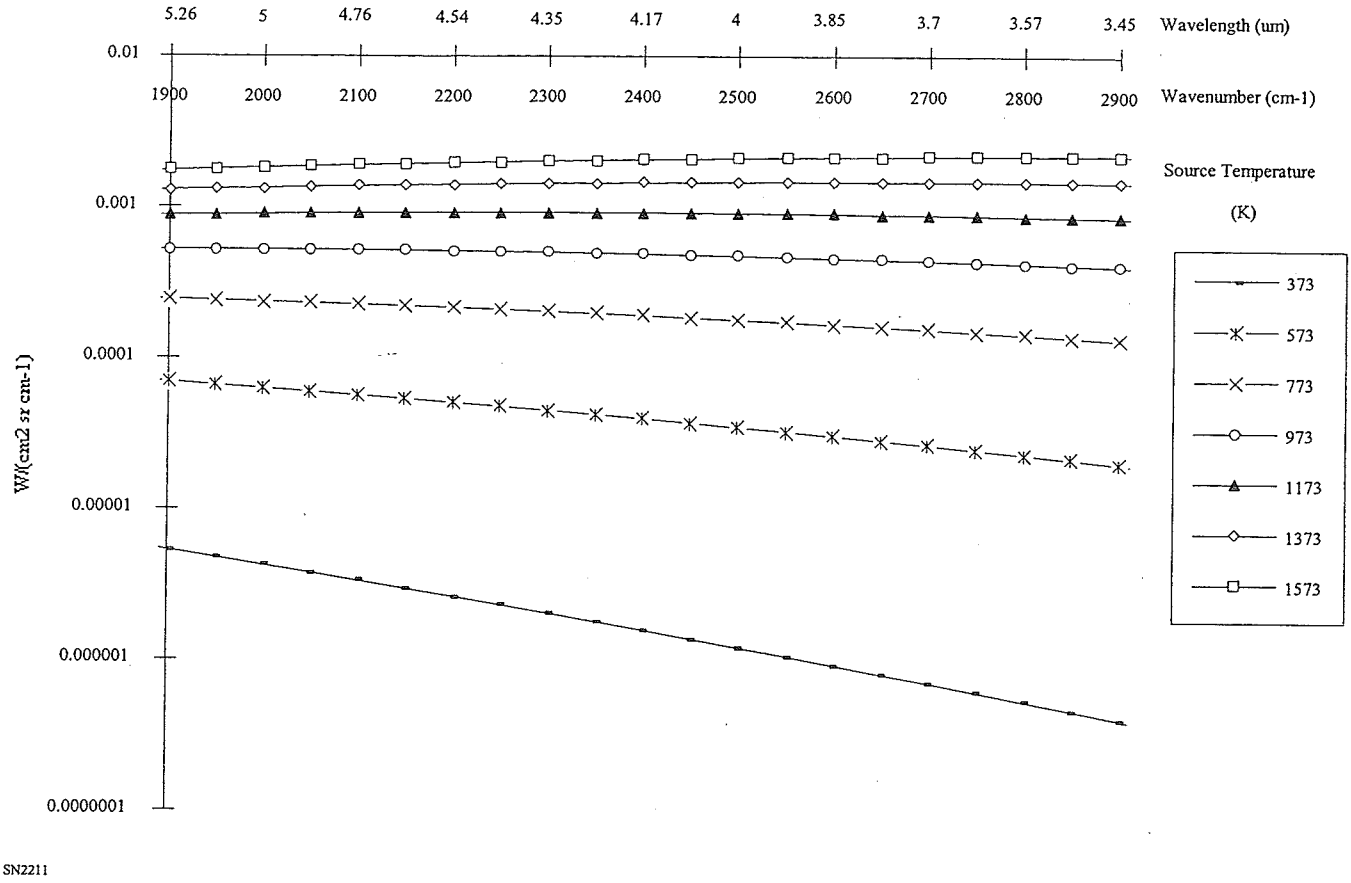

Figure 16. Scene spectral radiance vs. temperature

3.1.3 Transmission of the spectroradiometer

Transmission of the spectroradiometer is the ratio of the radiant signal at the detector to that at the input port, taking into account the reflectivity of mirrors and transmission through windows, beamsplitter, and lenses. The description and transmission coefficient of these elements is given in table 4. The system transmission $T(\sigma)$ (no units) is given by:

$$T(\sigma) = \prod_{i=1}^{n} \varepsilon_i(\sigma) \qquad (4)$$

where

$\varepsilon_i(\sigma)$ is the spectral transmission efficiency of element i (no units).

For the MR system, the standard beamsplitter is ZnSe, a nonhygroscopic material well adapted to field applications. The optical components of the MR systems along with their transmittance is

presented in table 4. The total estimated system transmission is about 30%. This transmission can be improved to about 50% by using an anti-reflection coating on the protective windows, however, this would have a detrimental effect on the spectral range coverage. Another way to improve the transmission is to use different window materials, unfortunately most good infrared window materials (Kbr, Kcl ...) are hygroscopic and require more care than ZnSe (see handling and care of hygroscopic materials if your system was ordered with hygroscopic optics).

It is interesting to note that the signal from interferometer input B goes through the beamsplitter substrate twice so the transmission loss is twice that of input A (see figure 1).

Table 4. Optical transmission of MR systems

Description	MR100 Transmission ZnSe	MR200 Transmission ZnSe	MR200 Transmission KBr
Flat Folding Mirror	.96	.96	.96
Parabolic Mirror	.96	.96	.96
Protective Window (Uncoated)	.69	.69	.92
Total Input Optics	**.64**	**.64**	**.85**
Cube-corner (3 reflections)	$.96^3$	$.96^3$	$.96^3$
Beamsplitter (input A)	.95	.95	.95
Output Optics Folding Mirror	.96	.96	.96
Total Interferometer Optics	**.81**	**.81**	**.81**
Protective Output Window (Uncoated)	.69	.69	.92
Parabolic Mirror	.96	.96	.96
Spherical Mirror	.96	.96	.96
Flat Folding Mirror	.96	.96	.96
Flat Folding Mirror	.96	-	-
Vacuum Window (MgF_2 for InSb)	-	.99	.99
Elliptic Mirror	.96	-	-
Plano-Convex CsI lens	-	.86	.86
Dewar Window (CaF_2 for InSb)	.95	-	-
Total Output Optics	**0.53**	**0.52**	**0.69**
Total System Transmission	**0.27**	**0.27**	**0.48**

3.1.4 Throughput

The throughput of the MR system is 0.004 cm^2 sr. Note also that the system can be used without having to reduce the throughput to a spectral resolution below 1 cm^{-1}.

3.1.5 Power at the Detector

The power at the detector (W/cm^{-1}) is given by:

$$P^{\text{detector}}(\sigma) = \frac{L(\sigma) \cdot T(\sigma) \cdot \Theta}{2} \qquad (5)$$

where

$T(\sigma)$ is the spectral instrument transmission efficiency (no units),

$L(\sigma)$ is the spectral radiance from the scene ($W/cm^2\ cm^{-1}$ sr),

Θ is the instrument throughput (cm^2 sr).

The evaluation of the power at the detector takes into account that the energy from input port 1 is divided equally between the two output ports (factor of 2 in equation 5).

3.1.6 Detector Current

The detector's responsivity is the detector output current for a given input illumination power. The responsivity is directly proportional to the wavelength multiplied by the quantum efficiency $\eta(\sigma)$. This is because shorter wavelength photons have more energy per photon and therefore there are fewer photons per watt of flux (either signal or background). The responsivity is thus dependent on the spectral frequency.

3.1.7 Sources of Noise

Noise refers to any electrical output other than the desired signal. Some noise sources are fundamental, and for several reasons cannot be avoided. A few of these reasons are:

- Photons do not arrive at a constant rate.
- Atoms in the detector vibrate slightly.
- Electrons move randomly.

Other noise sources arise externally and can be minimised, e.g.:

- electrical interference
- temperature fluctuation
- vibration that causes electrical components to shift

3.1.8 Photon Noise

Photon noise or shot noise is unavoidable; it is due to the random arrival of photons at the detector. Photon noise ($A/\sqrt{Hz}$) for a photovoltaic detector (InSb) is given by:

$$I^{photon} = \sqrt{2 \cdot e \cdot I^{detector}} \qquad (6)$$

It becomes $I^{photon} = \sqrt{e \cdot I^{detector}}$ for a photoconductor (MCT).

Although photon noise seems smaller in the case of a photoconductor detector than in a photovoltaic one, the sensitivity of photoconductors is relatively speaking, less.

Because photon noise is unavoidable, it is the ultimate limiting factor of the system's performance (SNR). Whenever possible, all other sources of noise should be kept lower than the photon noise.

Other sources of noise, such as the Johnson noise from the first amplifier stage feedback resistor, quantization noise, and detector dark noise contribute to the total noise.

3.1.9 Johnson Noise (InSb detectors)

The Johnson noise ($A/\sqrt{Hz}$) of the feedback resistor of the first stage of amplification is given by:

$$I^{Johnson} = \alpha \cdot \sqrt{\frac{4kT}{R_f}} \qquad (7)$$

where

R_f is the feedback resistor (Ω),

k $= 1.38 \times 10^{-23}$ J/K is the Boltzmann constant,

α is the noise factor for imperfect resistors (no units), estimated by the manufacturer to be 1.5,

T is the temperature of the resistor (K).

In the MR design, Johnson noise never dominates the total noise of the system. It increases the total system noise by less than 10% with the coldest scene temperature and by even less as the scene temperature is increased.

3.1.10 Quantization Noise

Quantization noise ($A/\sqrt{Hz}$) arises from the finite size of the quantization steps of the analogue-to-digital converter (ADC). It is given by:

$$I^{quantization} = \frac{R}{G \cdot 2^N \cdot \sqrt{12} \cdot \sqrt{f_N}} \qquad (8)$$

where

R is the range of the ADC (V),

G is the gain from detector to quantization (Ω),

N is the number of bits for quantization (no units),

f_N is the Nyquist frequency, which is half the sampling frequency (Hz).

Quantization noise is of concern in systems used to observe scenes of high radiance, such as the sun.

3.1.11 Dark Noise

Dark noise is the electronic noise observed when no radiation reaches the detector. This noise depends on the type of detector and the electronic circuitry used. The values used in the case of an InSb detector are 1.5×10^{-14} $A/\sqrt{Hz}$ for each detector. As for the quantization noise, dark noise in MR systems remains a negligible contributor to system noise.

3.1.12 Jitter Noise

Jitter noise is noise caused by jitter during sampling of the interferogram. Sampling jitter is mainly due to ADC jitter, laser intensity fluctuations, and the noise from the electronics that trigger the ADC.

Jitter noise can become troublesome at elevated scanning speeds. This is because at high speeds, a given jitter becomes non negligible as compared to the sampling interval. Jitter noise is especially annoying because it is proportional to the measured signal, therefore the SNR due to jitter cannot be improved by observing a warmer scene. Because of this rapid scanning systems require carefully designed electronic circuits to trigger the ADC. The reader is referred to [RD1] for more details.

3.1.13 Scanning Instability Noise

Scanning instability noise can be attributed to scanning speed instabilities together with uneven spectrometer response and/or a delay mismatch between the ADC triggering and the IR signal.

Mainly because of the analogue filter response at high frequencies, the MR spectroradiometer is operated with a non zero slope gain . This is not a problem if the scanning speed which converts optical speeds to electrical speeds is constant. This is not the case, however, and some noise-

equivalent current results from the peak amplitude of the speed variation and the analogue filter slope. Filter slope noise is often a non negligible contributor to FTIR system noise. This is why analogue filter design is carefully analysed with this limitation in mind.

Speed variations can also introduce noise if the ADC triggering circuitry is not perfectly synchronised with the IR signal. Because it has a larger bandwidth than the IR channel, the sampling laser fringe detection circuitry usually has a smaller associated delay. If this delay mismatch is not corrected for, the spectroradiometer will sample the interferogram with a constant negative time offset -Δt. This is not a problem if the scanning speed is constant. But as this is not the case, the uneven sampling resulting from the delay mismatch and speed variations converts into a noise-equivalent current.

Like jitter noise, these two sources of noise are especially annoying because they are proportional to the measured signal, so that the SNR due to these sources cannot be improved by observing warmer scenes. Careful design of the analogue filter cut-off frequency as well as delay mismatch compensation are therefore applied. The reader can refer to [RD1] for more details.

3.1.14 Instrument Efficiency

The modulation efficiency of the interferometer depends on many factors, such as the imperfections of the beamsplitter, and the shear and tilt of the recombining wavefronts. Modulation due solely to the imperfections of the beamsplitter is given by:

$$M_{BS}(\sigma) = 4\ r_{BS}(\sigma) \cdot t_{BS}(\sigma) \qquad (9)$$

where:

M_{BS} is the beamsplitter modulation,

r_{BS} is the beamsplitter reflectivity,

t_{BS} is the beamsplitter transmissivity.

Maximum beamsplitter modulation, i.e. $M_{BS} = 1$, occurs when r_{BS} and t_{BS} are equal to 0.5.

The typical interferometer modulation for input port A is 70% using 5-second precision corner-cube retroreflectors. Better modulation can be expected with the use of 1-second precision retroreflectors.

It should be noted that the total energy is split between the two output ports. This factor is normally included in the instrument efficiency ξ together with beamsplitter modulation and system transmission.

$$\xi = \frac{T(\sigma) \cdot M_{BS}}{2} \qquad (10)$$

Input port B can be set to look at a cold source to reduce the photon noise.

.3 NESR

The system's noise equivalent spectral radiance (NESR) (W/cm^2 sr cm^{-1}) is given by:

$$NESR = \frac{\sqrt{\left(\left(I^{photon}\right)^2 + \left(I^{quantization}\right)^2 + \left(I^{darknoise}\right)^2 + \left(I^{Johnson}\right)^2 + \left(I^{jitter}\right)^2 + \left(I^{scan.inst}\right)^2\right)}}{\Delta\sigma \cdot \Theta \cdot \xi \cdot \sqrt{t} \cdot R(\sigma) \cdot F} \qquad (11)$$

where

I^{photon} is the noise current due to photon noise ($A/\sqrt{Hz}$),

$I^{quantization}$ is the noise current due to quantization noise ($A/\sqrt{Hz}$),

$I^{Johnson}$ is the noise current due to the Johnson noise of the resistance of the first amplification stage ($A/\sqrt{Hz}$),

$I^{darknoise}$ is the noise current due to dark noise ($A/\sqrt{Hz}$),

I^{jitter} is the noise current due to the jitter of the sampling ($A/\sqrt{Hz}$),

$I^{scan.\ inst.}$ is the noise current due to scanning speed variations in the spectroradiometer, together coupled with the analogue filter slope and the delay mismatch ($A/\sqrt{Hz}$),

t is the acquisition time (s),

$\Delta\sigma$ is the spectral interval (cm^{-1}),

ξ is the instrument efficiency (no units),

$R(\sigma)$ is the responsivity of the system (A/W),

Θ is the instrument throughput (cm^2 sr),

F is the noise reduction apodization factor (no units), equal to 1 if no apodization is used.

Being incoherent, the various sources of noise are added in an RSS manner in equation 11.

3.1.16 Signal-to-Noise Ratio

Finally, the signal-to-noise ratio SNR is given by:

$$SNR(\sigma) = \frac{P(\sigma)}{NESR} \qquad (12)$$

3.2 Instrument Line Shape and Spectral Resolution

3.2.1 Instrument Line Shape

The ILS (instrument line shape) is the response of the spectrometer to a monochromatic spectral stimulus. This is illustrated schematically in figure 17. A distinct ILS spanning from $\sigma = -\infty$ to $+\infty$ exists for each wavenumber σ', although it changes from one σ' to the next in a slow and progressive manner. The ILS at a given wavenumber σ' represents the noiseless spectrum that would be obtained if the spectrometer were submitted to monochromatic radiation, for example that of a laser at $\lambda' = 1/\sigma'$. The ILS function $ILS_{\sigma'}(\sigma)$ is thus characterised by two indices, σ and σ', as illustrated in figure 17.

An observed spectrum $S^{observed}(\sigma)$ is the convolution of the ILS functions with the spectral distribution of photon incidence $B(\sigma)$.

$$S^{observed}(\sigma) = \int_{-\infty}^{\infty} B(\sigma - \sigma') ILS_{\sigma-\sigma'}(\sigma')\, d\sigma' \qquad (13)$$

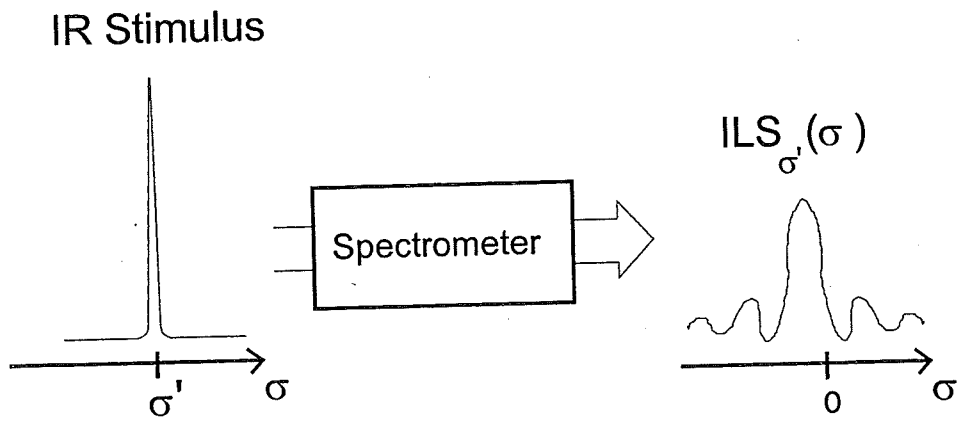

Figure 17. Monochromatic IR stimulus and instrumental response function (ILS)

If the spectral features or variations of $B(\sigma)$ are much wider than the width of the ILS peak, then $S^{observed}(\sigma)$ will be very similar to $B(\sigma)$. On the other hand, if $B(\sigma)$ has features much narrower than the ILS, $S^{observed}(\sigma)$ will be greatly affected by the response of the system. This is often referred

to as underresolving. In this case, the narrow lines from $B(\sigma)$ would all have widths very similar to that of the ILS. In the limiting case of an isolated monochromatic line, the measured spectrum is the ILS itself, as illustrated in figure 17.

From the viewpoint of the instrument, many parameters influence the ILS, such as the finite mirror scan length, the finite divergence in the interferometer, the IR alignment, and so on.

3.2.2 Spectral Resolution

In the present system, the width of the ILS is mainly governed by the extent of the finite length of the interferogram. For a system with negligible divergence and which is equipped with a round detector, the normalised ILS is given by:

$$ILS(\sigma', \sigma) = \frac{Sin(2\pi\sigma MPD)}{2\pi\sigma MPD} \qquad (14)$$

The ILS function due to the finite interferogram length is *independent of* σ, i.e. it is the same for all wavenumbers. This ILS function is illustrated in figure 17. The line shape seen in figure 18 is very similar to the actual simulated ILSs displayed in figure 17.

The FWHM of the ILS given by equation 15, $FWHM_{boxcar}$, can be derived analytically and is:

$$FWHM_{boxcar} = \frac{1.207}{2MPD} \qquad (15)$$

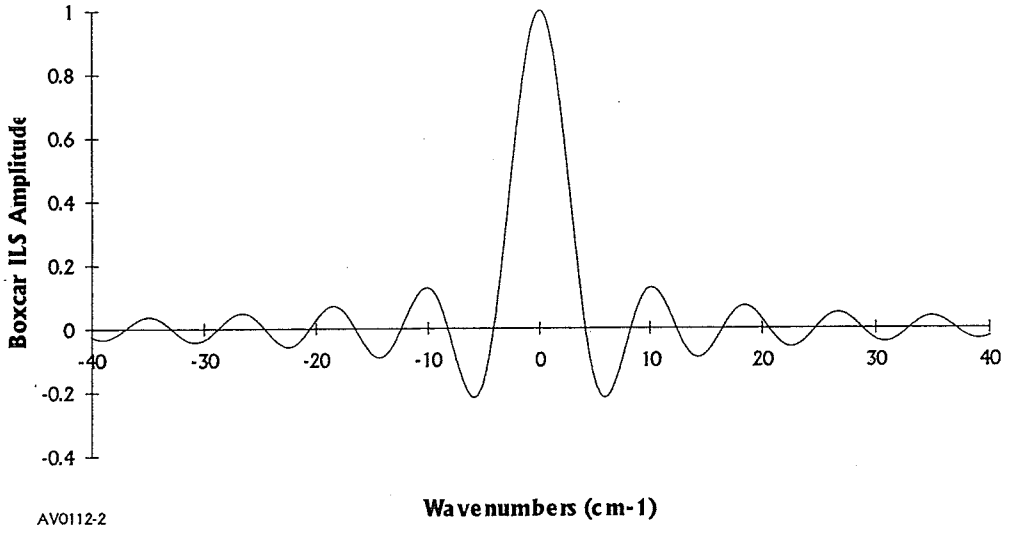

Figure 18. Plot of $\sin(2\pi\sigma L)/(2\pi\sigma L)$ (where L = 0.122 cm)

For an MPD of 0.122 cm, the sole contribution of the finite interferogram length to the resolution yields 4.96 cm^{-1}. The actual FWHM of the ILS can be written as:

$$FWHM_{ILS} = \beta \frac{1.207}{2MPD} \qquad (16)$$

where

β is a broadening factor to account for parameters other than the finite interferometer length.

The broadening factor β is mainly due to the finite divergence in the interferometer, a contribution which incidentally varies with the wavenumber, being larger for higher wavenumbers.

3.2.3 Apodization

As stated in the previous sections, the ILS is governed mainly by the finite interferogram length and thus closely resembles a Sin(x)/x function as seen in figure 18. This function is sometimes considered disadvantageous because it has amplitude oscillations which are large (21% for the first ripple), and which die off very slowly. It is possible to reduce the oscillations of the ILS by using post-acquisition digital processing on the acquired interferogram prior to Fourier transformation. This is referred to as *apodization* or "removal of feet", since the purpose of the operation is to remove or reduce the oscillations. This improvement of the ILS is gained at the cost of spectral resolution or increased ILS FWHM. The reader is referred to [RD1], pages 15-25, for an illustration of oscillation reduction. The effect of various types of apodizing functions on the ILS FWHM is illustrated in figure 19. Triangular, Hamming, and Gaussian functions are commonly used apodization functions. Boxcar apodization is the use of no apodizing function. For a given MPD, one can see in figure 19 that the ILS FWHM for boxcar apodization is better than that obtained using triangular, Hamming, or Gaussian apodization by a factor of 1.47, 1.52, and 1.68, respectively.

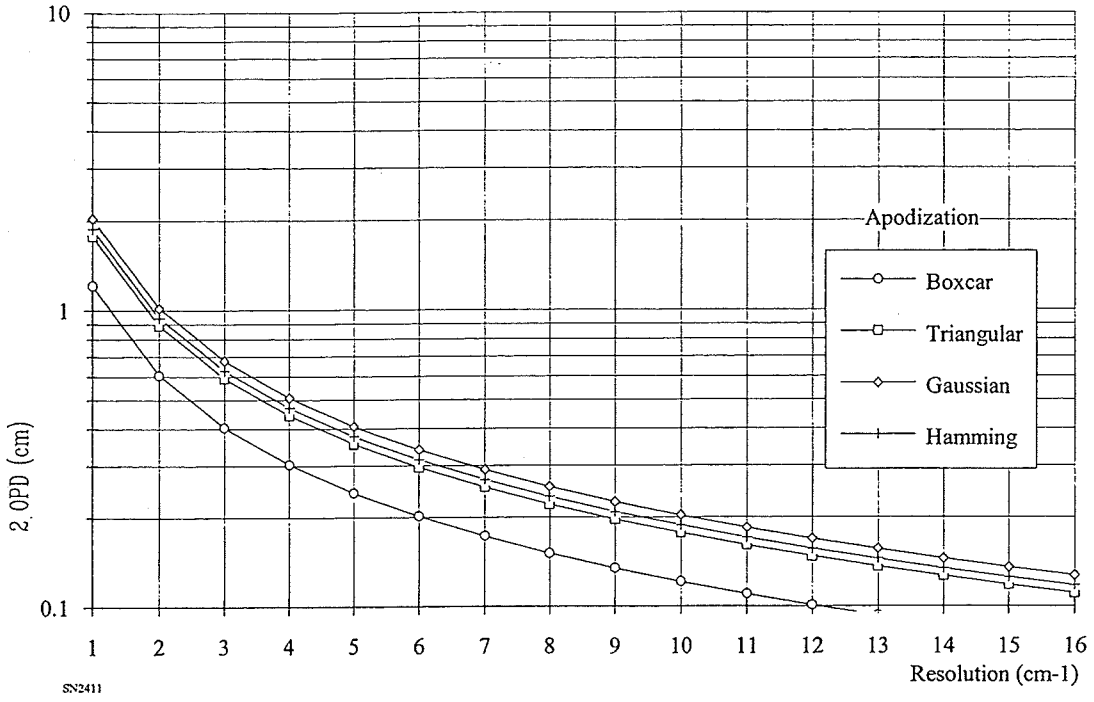

Figure 19. Optical path vs. resolution setting

3.3 Radiometric Calibration

Radiometers with no spectral capability, whether they are single-pixel or imaging systems, are notoriously difficult to calibrate radiometrically. The main reason for this is that at the detector level, a radiometer *integrates the radiant signal over a certain spectral range* and produces a single output. The integration translates into a loss of information, which limits the interpretation of the measurement.

The measurement produced by a radiometer is intended to be the radiance of a scene integrated over a specific spectral range. The actual output of a radiometer, however, is the radiance of the scene integrated over a specific spectral range but weighted by the *spectral response of the system*. Even after calibrating with a source of known radiance, e.g. a calibration blackbody, the uncertainty of the spectral response of the system induces an uncertainty in the intended measurement. This is because the response of the system is never flat within the spectral bandpass, and thus spectrally varying scenes of different integrated radiances can produce the same output. In other words, uneven spectral responses are linked with radiometric errors.

Spectroradiometers represent an improvement over non spectral radiometers. First, the addition of many spectral channels contributes to the narrowing of each channel, thus potentially making each of them more uniform. Another advantage is that it may be possible to restore distorted signals. If spectral channels are located in a contiguous manner, spectrally side-by-side, an over-evaluation of a given channel is accompanied by the complementary under-evaluation in neighbouring channels. This

means that the correct radiance of a feature in the spectrum can be evaluated by spectrally integrating over all channels which responded to the signal. Spectroscopically, this is a known phenomenon. When a spectrometer is operated at a resolution lower than the intrinsic features of a scene, the representation of these features in the spectrum is broader and weaker, but the integrated intensity is correct.

Consequently, the radiometric characterisation of FTIR-based spectroradiometers is a straightforward operation that leads to a radiometrically sound calibration. This is due to the intrinsically large number of spectral channels in FTIR-based systems. In fact the spectral response of a channel is given by the ILS function described in the previous section. An FT-based spectroradiometer has a large number of overlapping and smoothly varying channels.

3.3.1 Calibration Theory

The ideal radiometer is a *linear instrument*, i.e. the measured signal for each pixel and each spectral channel is proportional to the radiant spectral power at the detector. This is illustrated in figure 20. The power at the detector is composed of two contributions, the spectral power from the scene, and that from the thermal emission of the spectrometer itself. Because of this, the response line in figure 20 does not cross the abscissa at x = 0 but rather at some value corresponding to the thermal emission of the spectrometer. A calibration for such a system thus requires a least two measurements as illustrated by the ×'s in figure 20. If the emission of the instrument could be neglected, only one characterisation measurement would be necessary.

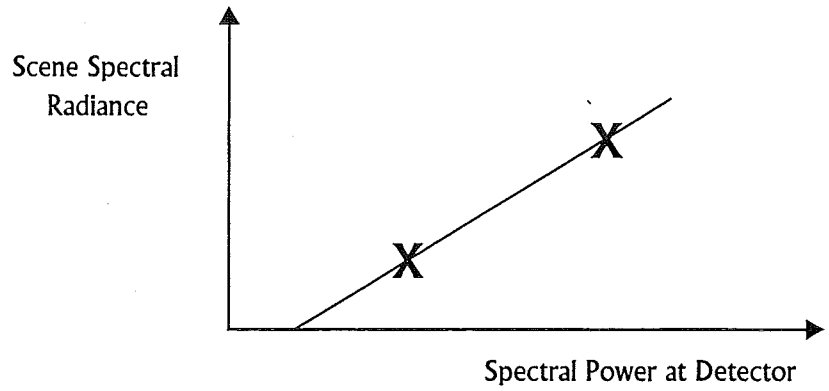

Figure 20. Linear relationship between the scene spectral radiance and the power at the detector.

Let us now look at the calibration equations. An uncalibrated measurement can be expressed as:

$$S^{Measured}(\sigma) = K(\sigma)\left(L^{Source}(\sigma) + M^{Stray}(\sigma)\right) \quad (17)$$

where

$S^{Measured}(\sigma)$ is the measured complex spectrum (arbitrary),

$K(\sigma)$ is the complex instrument response function (arbitrary cm^2 sr cm^{-1}/W),

$L^{Source}(\sigma)$ is the source spectral radiance (W/cm^2 sr cm^{-1}),

$M^{Stray}(\sigma)$ is the spectral power of the stray radiance (W/cm^2 sr cm^{-1}).

An interferogram always has a certain degree of asymmetry due to dispersion present in the beamsplitter (the wavelength-dependent refractive index) and in the amplification stages of the detectors (the frequency-dependent electronic delays). This asymmetry causes the Fourier transform of the interferogram (i.e. the spectrum) to have an imaginary part. At this point a phase correction can be applied to the complex spectrum to yield a real spectrum. With the present calibration algorithm, however, the phase correction is not needed and instead we can work with complex spectra.

A radiometric calibration is a two-step process. First, the two unknowns per detector *radiometric gain* $K(\sigma)$ and *radiometric offset* $M^{Stray}(\sigma)$, are determined using an experimental step called a *characterisation*. Second, the *calibration* is applied to an uncalibrated measurement to produce a calibrated spectrum.

The gain and offset characterisation requires two measurements, one hot blackbody measurement and one cold blackbody measurement, ideally both uniformly filling the field of view. This is referred to as a *two-point calibration* (as discussed earlier and as seen in figure 20). The temperatures of the calibration blackbody measurements are judiciously set in order to minimise calibration error.

Applying equation 17 to the measurements of the hot and cold blackbodies, we get the following equations:

$$L_H(\sigma) = S_H^{Measured}(\sigma) / K(\sigma) - M^{Stray}(\sigma) \quad (18)$$

$$L_C(\sigma) = S_C^{Measured}(\sigma) / K(\sigma) - M^{Stray}(\sigma) \quad (19)$$

where

$L_H(\sigma)$ and $L_C(\sigma)$ are the theoretically calculated spectral radiances using the emissivity of the blackbody and the Planck function at the temperature of the blackbody:

$$L_x(\sigma) = \varepsilon_x(\sigma)\, P_{T_x}(\sigma) = \varepsilon_x(\sigma)\, \frac{C_1 \sigma^3}{\exp\left(\frac{C_2 \sigma}{T_x}\right) - 1} \qquad (20)$$

where

$\varepsilon_x(\sigma)$ is the emissivity of the x blackbody,

x = C for the cold blackbody and H for the hot blackbody,

C_1 = 1.191 x 10^{-12} W cm^2 and is the first radiation constant,

C_2 = 1.439 K cm and is the second radiation constant,

σ is the wavenumber (cm^{-1}) and

T_x is the temperature of the x blackbody (K).

The solution to equations 18 and 19 yields equations 21 and 22. It is then simple to solve for the two unknowns $K(\sigma)$ and $M^{stray}(\sigma)$.

$$K(\sigma) = \frac{S_H^{Measured}(\sigma) - S_C^{Measured}(\sigma)}{L_H(\sigma) - L_C(\sigma)} \qquad (21)$$

$$M^{Stray}(\sigma) = \frac{L_H(\sigma) \cdot S_C^{Measured}(\sigma) - L_C(\sigma) \cdot S_H^{Measured}(\sigma)}{S_H^{Measured}(\sigma) - S_C^{Measured}(\sigma)} \qquad (22)$$

The calibrated spectrum is given by:

$$S^{Calibrated}(\sigma) = S^{Measured}(\sigma) K^{-1}(\sigma) - M^{Stray}(\sigma) \qquad (23)$$

This method assumes that the operating parameters are not changed between the measurement of the calibration spectra and that of the scene spectra. The scanning speed and the optical configuration must remain the same. Since the experiment requires the acquisition of data in both directions of the interferometer stroke, two sets of $M^{Stray}(\sigma)$ and $K(\sigma)$ must be provided (one for each direction) for the calibration.

The radiometrically corrected measurements are also complex spectra. However, all spectral information should be contained in the real part of the complex spectra. The imaginary part should only contain noise. The imaginary part can be used to validate the spectra and to estimate the noise levels. After verification, the imaginary part can be dropped to free up storage space.

3.3.2 Multiple Point Calibrations

The calibration procedure can be extended to use multiple reference points instead of two points. Multiple point calibrations are used to improve the quality of the obtained calibrated spectra. There are two types of error that can be addressed by multiple point calibrations, random errors due to noise and systematic errors due to non-linear response of the spectroradiometer (see section 3.4.4).

3.3.2.1 Linear Multiple Point Calibrations

Linear multiple point calibrations are used to reduce the impact of random uncertainty on the calibration curve. When a series of measurements are taken for black bodies at different temperatures there is always a fluctuation around the ideal calibration line as shown in figure 21.

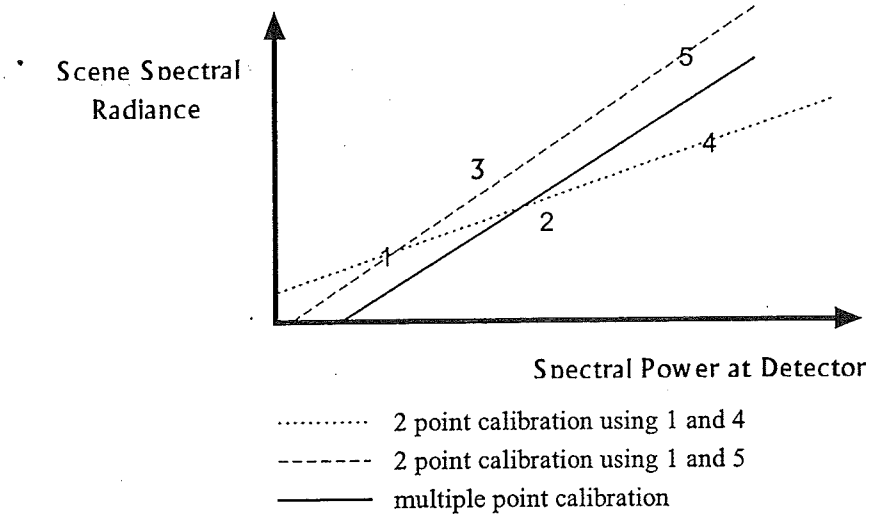

Figure 21. Multiple point linear relationship between the scene radiance and the detector response.

The best calibrated spectra will be obtained by using the multiple point calibration which is a linear regression that uses all the available points in order to more accurately characterise the system. If we apply equation 17 to the measurements of multiple black bodies we get the following system of equations:

$$\begin{aligned} L_1(\sigma) &= S_1^{Measured}(\sigma)/K(\sigma) - M^{Stray}(\sigma) \\ L_2(\sigma) &= S_2^{Measured}(\sigma)/K(\sigma) - M^{Stray}(\sigma) \\ &\text{M} \\ L_n(\sigma) &= S_n^{Measured}(\sigma)/K(\sigma) - M^{Stray}(\sigma) \end{aligned} \qquad (24)$$

The above equations form a system of linear equations. The general solution to such a system for n equations is as follows :

$$K(\sigma) = \frac{n\sum_i S_i^{Measured}(\sigma)^2 - \left(\sum_i S_i^{Measured}(\sigma)\right)^2}{n\sum_i S_i^{Measured}(\sigma)L_i(\sigma) - \sum_i S_i^{Measured}(\sigma)\sum_i L_i(\sigma)} \quad (25)$$

$$M^{Stray}(\sigma) = \frac{n\sum_i S_i^{Measured}(\sigma)\sum_i S_i^{Measured}(\sigma)L_i(\sigma) - \left(\sum_i S_i^{Measured}(\sigma)\right)^2 \sum_i L_i(\sigma)}{n^2\sum_i S_i^{Measured}(\sigma)^2 - n\left(\sum_i S_i^{Measured}(\sigma)\right)^2} - \frac{\sum_i L_i(\sigma)}{n} \quad (26)$$

Equations 25 and 26 can be used to solve for systems of equations in the form of equation 24. In the case illustrated in figure 21 n equals 5 and *i* runs from 1 to 5. The calibrated spectrum is then given by equation 23 as before.

3.3.2.2 Non-Linear Multiple Point Calibrations

Non-linear multiple point calibrations are used to correct for non-linearities in the response function of the FT spectroradiometer.

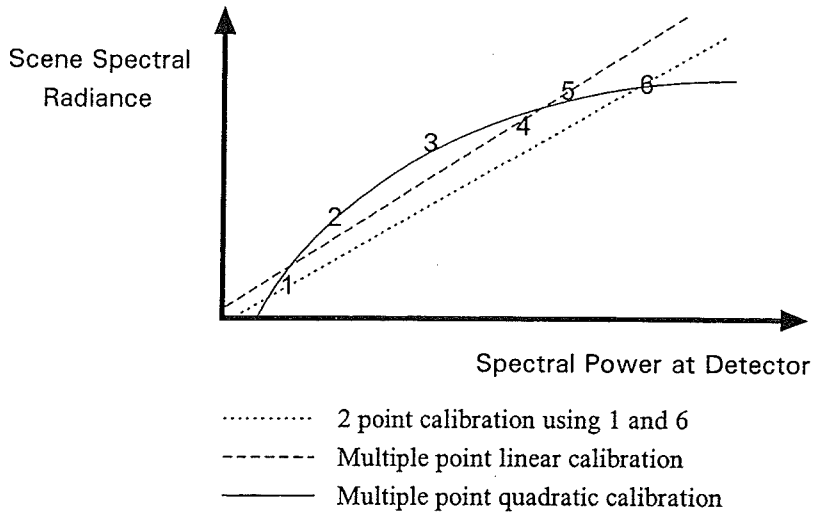

Figure 22. Non linear relationship between the scene radiance and the detector response.

The idea is to model the non-linear response of the system by using a quadratic function instead of a linear function. The uncalibrated measurement is now expressed as :

$$S^{Measured}(\sigma) = Q(\sigma)\left(L^{Source}(\sigma) + M^{Stray}(\sigma)\right)^2 + K(\sigma)\left(L^{Source}(\sigma) + M^{Stray}(\sigma)\right) \quad (27)$$

where

$S^{Measured}(\sigma)$ is the measured complex spectrum (arbitrary),

$Q(\sigma)$ is the non-linear instrument response function (arbitrary (cm^2 sr $cm^{-1}/W)^2$),

$K(\sigma)$ is the complex instrument response function (arbitrary cm^2 sr cm^{-1}/W),

$L^{Source}(\sigma)$ is the source spectral radiance (W/cm^2 sr cm^{-1}),

$M^{Stray}(\sigma)$ is the spectral power of the stray radiance (W/cm^2 sr cm^{-1}).

The radiometric calibration is performed as before but there are now three unknowns per detector, the *non-linear radiometric gain* $Q(\sigma)$, the *linear radiometric gain* $K(\sigma)$ and the *radiometric offset* $M^{Stray}(\sigma)$. This non-linear *calibration* is then applied to an uncalibrated measurement to obtain a calibrated spectrum.

The characterization of the above system requires a minimum of three different temperature blackbody measurements. If we apply equation 27 to the three measured blackbodies we get the following system of equations.

$$S_1^{Measured}(\sigma) = Q(\sigma)\left(L_1^{Source}(\sigma) + M^{Stray}(\sigma)\right)^2 + K(\sigma)\left(L_1^{Source}(\sigma) + M^{Stray}(\sigma)\right) \quad (28)$$

$$S_2^{Measured}(\sigma) = Q(\sigma)\left(L_2^{Source}(\sigma) + M^{Stray}(\sigma)\right)^2 + K(\sigma)\left(L_2^{Source}(\sigma) + M^{Stray}(\sigma)\right) \quad (29)$$

$$S_3^{Measured}(\sigma) = Q(\sigma)\left(L_3^{Source}(\sigma) + M^{Stray}(\sigma)\right)^2 + K(\sigma)\left(L_3^{Source}(\sigma) + M^{Stray}(\sigma)\right) \quad (30)$$

It is now possible to solve for the three unknowns $Q(\sigma)$, $K(\sigma)$ and $M^{Stray}(\sigma)$. The calibrated spectrum is then given by :

$$L^{Source}(\sigma) = \frac{\left(K(\sigma) - 2Q(\sigma)M^{Stray}(\sigma)\right)}{2Q(\sigma)} \pm \frac{\sqrt{\left(2Q(\sigma)M^{Stray}(\sigma) + K(\sigma)\right)^2 - 4Q(\sigma)\left(Q(\sigma)M^{Stray}(\sigma) + K(\sigma)M^{Stray}(\sigma) - S^{Measured}(\sigma)\right)}}{2Q(\sigma)} \quad (31)$$

This algorithm can be extended to more than three points using statistical regression analysis on the polynomial much in the same way as was done for the linear case.

3.4 Radiometric Accuracy

Radiometric accuracy is the deviation of the measured spectral radiance from the actual scene radiance. This is illustrated schematically in figure 23.

Strictly speaking, even if noise[1] affects the radiometric accuracy, it is treated as a separate parameter, the NESR, and is not included in the radiometric accuracy.

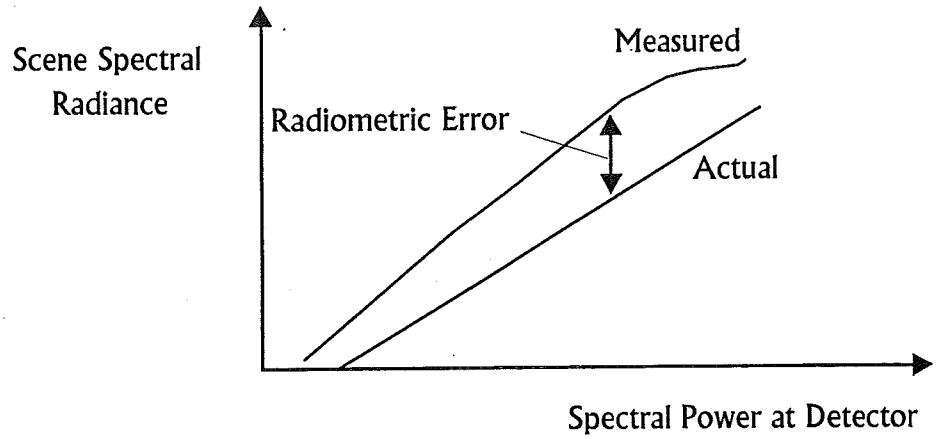

Figure 23. Actual and measured scene spectral radiance vs spectral power at the detector.

In general, radiometric accuracy is an arbitrary function as seen in figure 23, but is usually described in two parts, one absolute, the other relative. Radiometric error is absolute, if it does not vary with the scene radiance, or relative, if the error does vary with scene radiance. Absolute errors are more difficult to estimate than relative ones. In the following paragraphs, we will only discuss relative

[1] The distinction between noise and radiometric error is somewhat arbitrary. We will assume that noise is the spectral-element to spectral-element uncorrelated intensity variations, which statistically average out with time. Radiometric errors stem from system imperfections and stay in the calibrated spectra even after all visible noise has been washed out.

radiometric errors, converting absolute errors into relative equivalents. This is a more convenient way to predict the system accuracy for a given scene.

Radiometric accuracy is influenced by three types of errors. The first type, *calibration source errors*, are deviations in the production of a perfect (i.e. perfectly known) calibration source. These errors include the accuracy of blackbody temperature and the accuracy of it's emissivity over the operational spectral range. The second type of error is *calibration drift*. Calibration drift includes everything which changes the radiometric gain and offset during the time interval between the performing of calibration measurements and scene measurements. Calibration drift is influenced by many factors including the ambient temperature, the stability of the electrical gain, the stability of detector responsivity, and opto-mechanical stability. Finally, the third type of error that influences radiometric accuracy is the spectrometer *intrinsic linearity*. This includes system parameters such as detector linearity, channel spectrum, and spectral aliasing.

Because they are uncorrelated, the contributions from all predicted errors add up in a root-sum-square fashion.

3.4.2 Calibration Source Errors

Calibration source errors are misevaluations of the spectral radiance supplied by the calibration source. The effect of calibration source errors is illustrated in figure 24. The calibration points on the graph are misplaced and the resulting calibration line is thus skewed.

There are two types of calibration source errors. The first is a misevaluation of the radiance supplied by the calibration source. This is known as *blackbody error*. Calibration source emissivity error and temperature error are of this type.

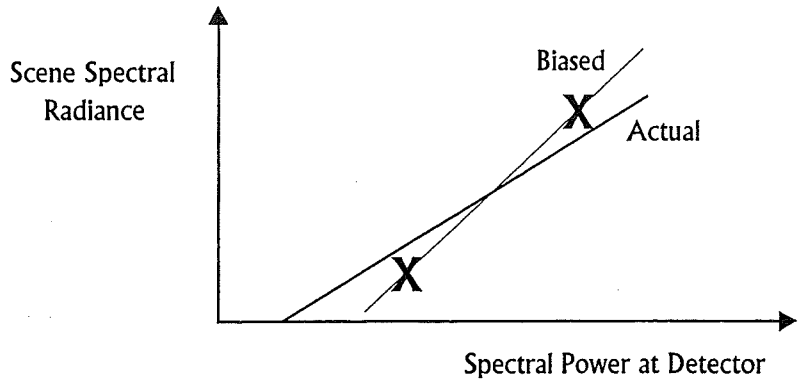

Figure 24. The effect of calibration source errors on radiometric calibration.

Emissivity is a factor contributing to blackbody errors. To analyse the effect of underestimating or overestimating blackbody emissivity, it is interesting to examine equations 21 and 22. When everything else is constant, the calculated radiometric gain is inversely proportional to the emissivity used for the blackbody. The calculated radiometric offset is, for its part, directly proportional to the emissivity used for the blackbody. These dependencies translate into a direct proportionality of a calibrated spectrum (equation 23) on the emissivity used for the blackbody. In other words, the use of 1%-inflated emissivity values leads to 1%-overestimated calibrated spectra, and thus 1% radiometric

errors. Good emissivity for available blackbodies in the 2000 to 2860 cm^{-1} (3.5 μm to 5 μm) spectral region is typically 0.98 ± 0.01. This is 1% emissivity accuracy.

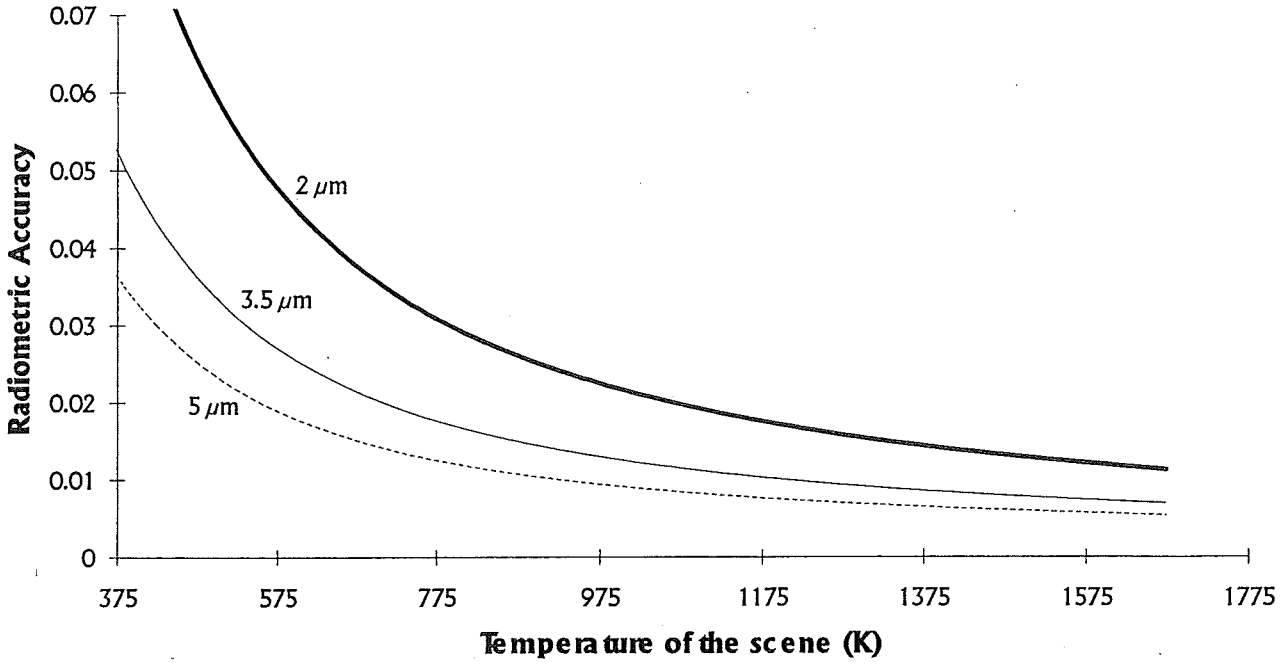

Figure 25. Relative radiometric errors at 5000 cm^{-1}, 2860 cm^{-1}, and 2000 cm^{-1} (2 μm, 3.5 μm, and 5 μm) due to the uncertainty of the calibration source temperature, assuming a blackbody relative temperature accuracy of 0.2% and an absolute accuracy of 1°

The error contribution due to temperature uncertainty is also important. Estimating the error in this case is more difficult, however, since it involves three Planck functions (equation 20), one evaluated at

T_H — the temperature of the hot blackbody, one evaluated at T_C — the temperature of the cold blackbody, and one evaluated at T_S — the temperature of the scene. For a particular choice of T_S, it is possible to find a certain combination of T_H and T_C to minimise the error. In general, however, we can say that the relative radiometric error due to calibration source temperature uncertainty will always be less than the values displayed in figure 25, as long as $T_H > T_S > T_C$. In other words, the values displayed in figure 25 are upper-limit relative radiometric errors due to calibration source temperature uncertainty. Here, we have assumed a relative blackbody temperature accuracy of 0.2% and an absolute accuracy of 1°. The maximum error is 5% for the coldest source (T_S = 373 K) at the highest frequency (σ = 2860 cm^{-1}). This is a very pessimistic value.

3.4.3 Calibration Drift

Calibration drift is the variation of radiometric gain and offset, between the time they are acquired (the characterisation) and the time they are applied (the scene measurement). This is illustrated schematically in figure 26.

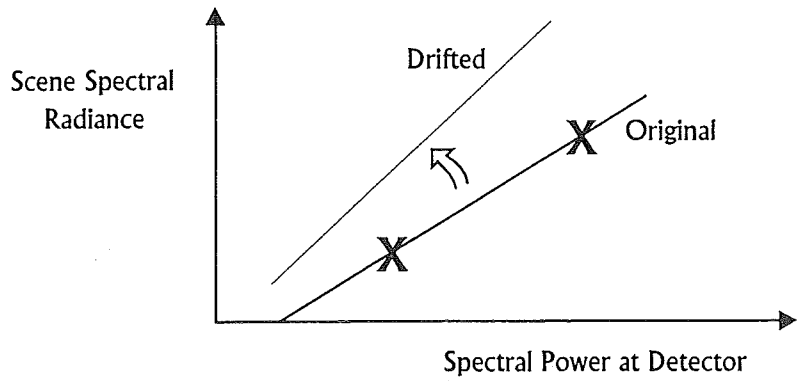

Figure 26. Relative radiometric error due to calibration drift.

We can write this relative radiometric accuracy, due to calibration drift, as:

$$RA^{Drift} \approx t \sqrt{\left(\frac{dG_E}{dt}\right)^2 + \left(\frac{dR_D}{dt}\right)^2 + \left(\frac{dG_O}{dt}\right)^2} \qquad (32)$$

where

t is the time interval between the characterisation and the scene measurement (s),

dG_E/dt is the relative rate of change of the electronic gain of the system (Hz),

dR_D/dt is the relative rate of change of the responsivity of the detector (Hz),

dG_O/dt is the relative rate of change of the system response due to optical alignment (Hz).

This equation applies to a case where drift varies linearly with respect to time, i.e. it always goes in the same direction. After a long period of time, equation 32 will overestimate the radiometric error. The three rates of change cited above are governed principally by the change of temperature of the instrument.

Unlike other detectors, such as MCT units, InSb detectors exhibit much less variation of responsivity with respect to temperature. DR_D/dt is then negligible compared with other sources of calibration drift, whether the detector is cooled with a liquid-nitrogen pour-filled Dewar or with a sterling cooler. This assumes, however, that the temperature of the detector remains below a certain temperature limit of about 120 K. In a mobile environment, where all directions are permitted, special care must be taken to ensure that none of the nitrogen is spilled if the Dewar is turned upside down.

dG_E/dt is affected by temperature drift as well as by electromagnetic disturbances, but these can be kept at a minimum through careful design and the use of high-quality components. $D\dot{G}_O/dt$ is very difficult to estimate, as it is influenced by a great number of design parameters. The ultimate test is, of course, to actually measure the drift experimentally.

One way to estimate the radiometric accuracy budget assigned to calibration drift is to examine the typical temporal drift of the MB100, the FTIR spectrometer on which the design of the MR system is based. The relative drift of the system response is 2% over a 16-hour period.[2] These results have been obtained with a system subjected to typical room-temperature fluctuations. However, it is probably possible to recalibrate more often than every 16 hours using a calibration source or other calibration references. For the MR system, we typically use 2% as the relative radiometric accuracy due to drift, and assume that the corresponding time interval between characterisation and scene measurement is long enough to allow measurement.

3.4.4 Intrinsic Linearity

The intrinsic linearity of the spectroradiometer pertains to errors other than calibration source errors and calibration drift errors. Typical non-linearity is illustrated in figure 27. In this case, the measured spectral radiance from the scene is accurate at the two calibration points and deviates from the true values when we move away from these points. For this type of error, it is advantageous to choose a calibration source temperature so the spectral radiance of the calibration measurements is included in the range of the spectral radiance to be measured. The exact location depends on the actual non-linear response.

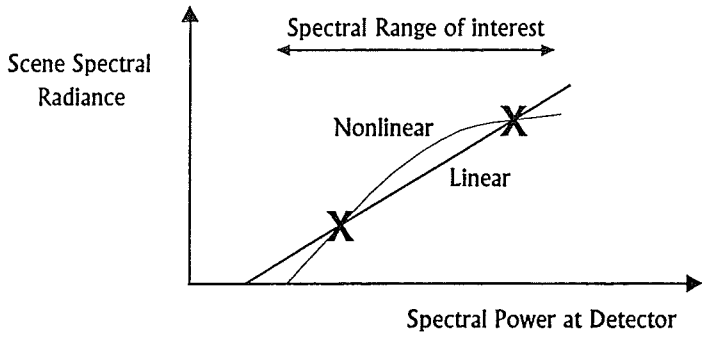

Figure 27. Relative radiometric error due to intrinsic linearity errors.

3.4.4.2 Detector Non-Linearity Error

Non-linearity is usually thought to be caused by detector responsivity non-linearity. Photoconductive MCT detectors are notorious for their non-linear response. On the other hand, photovoltaic InSb detectors, are usually operated in a regime where they are extremely linear. They start to saturate very quickly at an illumination level corresponding to a photogenerated current of about 200 μA per detector mm^2. In MR systems, the saturation level is never reached because the feedback resistors used are high enough so that preamplifier saturation occurs before there is detector saturation. We therefore do not anticipate detector non-linearity problems in InSb detectors.

---

[2] A good part of this drift is believed to be due to the variation of the internal source.

3.4.4.3 Channel Spectrum Error

Channel spectrum is spectral pollution that leads to a radiometric error. It manifests itself as a series of interference fringes appearing on top of an uncalibrated spectrum. Channel spectrum occurs when transmissive optical components with near-parallel flat faces are used. Interference fringes arise from constructive and destructive interference of internal reflected waves in the optical components.

Channel spectrum generates an oscillatory radiometric error of period $1/2tn$, where t is the plate thickness in centimetres and n is the index of refraction proportional to the spectral radiance. The relative radiometric accuracy due to channel spectrum is given by:

$$RA^{Channel} = 2R\, M_S M_T \qquad (33)$$

where

R is the single plate reflectivity of the plate,

$M_s \leq 1$ is the attenuation factor caused by the shearing of wavefronts,

$M_t \leq 1$ is the attenuation factor caused by the tilting of wavefronts.

Shearing wavefronts with respect to one another attenuates the interference. The shearing can be achieved by tilting the optical component. By doing so the main beam will shift by a certain amount which has to be compensated for by proper opto-mechanical realignment. As illustrated in figure 28, the secondary beam will shift from the main one by a quantity δ given in cm by:

$$\delta = 2t\ Cos\phi\ Tan\left[ArcSin\left(\frac{Sin\phi}{n}\right)\right] \qquad (34)$$

where

t is the thickness of the plate (cm),

ϕ is the angle of incidence of the incident beam (radians) and

n is the index of refraction of the plate.

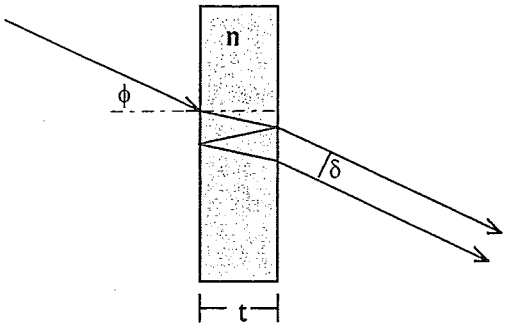

Figure 28. Shearing of the secondary beam in a tilted plate with parallel faces.

The attenuation factor caused by the shear is:

$$M_S = \frac{Sin(2\pi\sigma\theta\delta)}{2\pi\sigma\theta\delta} \qquad (35)$$

where

σ is the wavenumber of interest (cm^{-1}),

θ is the beam divergence half angle (radians) and

δ is the shear given by equation 34 (cm).

Parallel-face protective windows are included in MR systems right after the telescope and before the output optics. The level of channel spectrum generated by such a window is calculated using equation 33 with $M_T = 0$, and equations 34 and 35. A certain degree of wedging of this window would further reduce the channel spectrum but at the cost of introducing the phenomenon of *ghost images*. Ghost images are generated when reflections from the wedge's surfaces (of an off-axis source, which can be many times more intense than the source of interest (on-axis)), reach the detector and give an erroneous signal. This is illustrated schematically in figure 29.

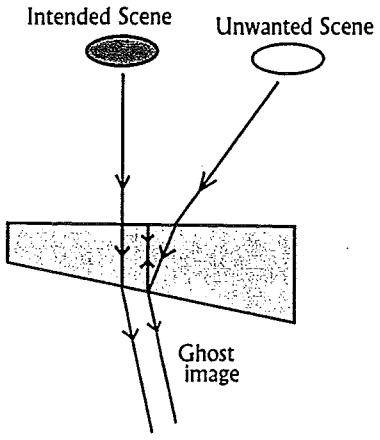

Figure 29. Ghost image phenomenon encountered with a wedged substrate.

Ghost images are especially annoying and must be avoided if possible.

3.4.4.4 Spectral Aliasing Error

Spectral aliasing is the folding over of all signal and noise within the bandpass of the system into the spectral free range which spans from 0 to the Nyquist frequency (half the sampling frequency). To avoid the overlapping of spectral features, it is important that any spectral information outside the spectral range of interest be removed. This can be done electrically with a low-pass filter, but this method does not provide a sharp cut-off over the upper limit of the frequency range or attenuation below the lower limit. A more appropriate method is to use an optical filter which provides both a sharp cut-off and very high attenuation outside the spectral range of interest. This method also reduces photon noise.